Supplementary material

Ultraviolet Light Blocking Optically Clear Adhesives for Foldable Displays via Highly Efficient Visible-Light Curing

Yonghwan Kwon,[1,†] Seokju Lee,[1,†] Junkyu Kim,[1] Jinwon Jun,[2] Woojin Jeon,[1] Youngjoo Park,[1] Hyun-Joong Kim,[3] Johannes Gierschner,[4] Jaesang Lee,[2,*] Youngdo Kim,[5,*] and Min Sang Kwon[1,*]

[1]Department of Materials Science and Engineering, Seoul National University, Seoul, Republic of Korea

[2]Department of Electrical and Computer Engineering, Seoul National University, Seoul, Republic of Korea

[3]Department of Agriculture, Forestry and Bioresources, Seoul National University, Seoul, Republic of Korea

[4]Madrid Institute for Advanced Studies, IMDEA Nanoscience, Calle Faraday 9, Campus Cantoblanco, 28049 Madrid, Spain

[5]Samsung Display Co., Ltd., Cheonan, Republic of Korea

e-mail: minsang@snu.ac.kr (M.S.K.), colour.kim@samsung.com (Y. K.), jsanglee@snu.ac.kr (J. L.)

Contents

Supplementary Note 1. General information

1.1. Chemicals

4DP-IPN, 4Cz-IPN and dimethyl 2-(4-(dimethylamino)benzylidene)malonate) (UVA-1) were synthesized according to the procedures previously reported by our group.[1–3] All chemicals and solvents for the syntheses were purchased commercially and used without further purifications. Ethyl 2-cyano-3,3-diphenylacrylate (UVA-2, TCI), 2-ethylhexyl acrylate (EHA, Aldrich), 4-hydroxybutyl acrylate (HBA, TCI), butyl acrylate (BA, Aldrich), 2-dimethylaminoethyl acrylate (DMAEA, Aldrich), 2-dimethylaminoethyl acetate (DMAEAc, TCI), [4-(Octyloxy)phenyl](phenyl)iodonium hexafluoroantimonate (HNu 254, TCI) and 2-butanoyloxyethyl(trimethyl)azanium butyl(triphenyl)boranuide (Borate V, Spectra Group Limited, Inc.) were purchased commercially. Acrylic monomers were purified by passing from basic alumina (Aldrich) to remove the inhibitors. Polyethylene terephthalate (PETE, 50 μm, youngwoo trading), release film (silicon-treated PETE film, 100 μm, youngwoo trading), super release film (silicon-treated PETE film, 100 μm, youngwoo trading) were purchased commercially.

1.2. General experimental procedures

■ General experimental procedures for synthesis of acrylic syrup

A 20 ml vial (glass, Sungho SIGMA) equipped with a stirring bar was charged with monomer mixture, PCs, and co-initiators. Afterwards, the vial was capped with a rubber septum and sealed with parafilm and bubbled with 99.999% N_2 for 30 min. PCs and co-initiators were used after dilution in acrylate monomers for the reproducibility. In the case of addition of UVAs, they were added in this reaction solution before bulk polymerization in newly designed PIS. During the bubbling, aluminum foil was used to block the room light to prevent undesired polymerization. Subsequently, acrylic syrup was synthesized under irradiation of 3W MR 16 light-emitting diode (LED) (λ_{max} = 455 nm, 25–100 mW/cm^2) at RT.

■ General experimental procedures for film curing

For film curing, two 15 W string-type blue LEDs (λ_{max} = 452 nm) were used, and their intensities were set up as 10 mW/cm^2. Film curing was carried out by additionally irradiating visible light to the prepared acrylic syrup. Since the PIS used in this process reuses the PC within the catalyst cycle of the acrylic syrup preparation process, no new additives were added during the film process. Moreover, a crosslinking agent was also not included in this process. For film curing, acrylic syrup was coated between two release films and casted to a thickness of 50 μm using a film casting applicator. The samples for measurements of optical and viscoelastic properties were cured for 40 min for the previous PIS (4Cz-IPN and tertiary amines) and 30 min for the new PIS (4DP-IPN, HNu 254 and Borate V) to obtain fully cured OCAs.

1.3. Instrumentation

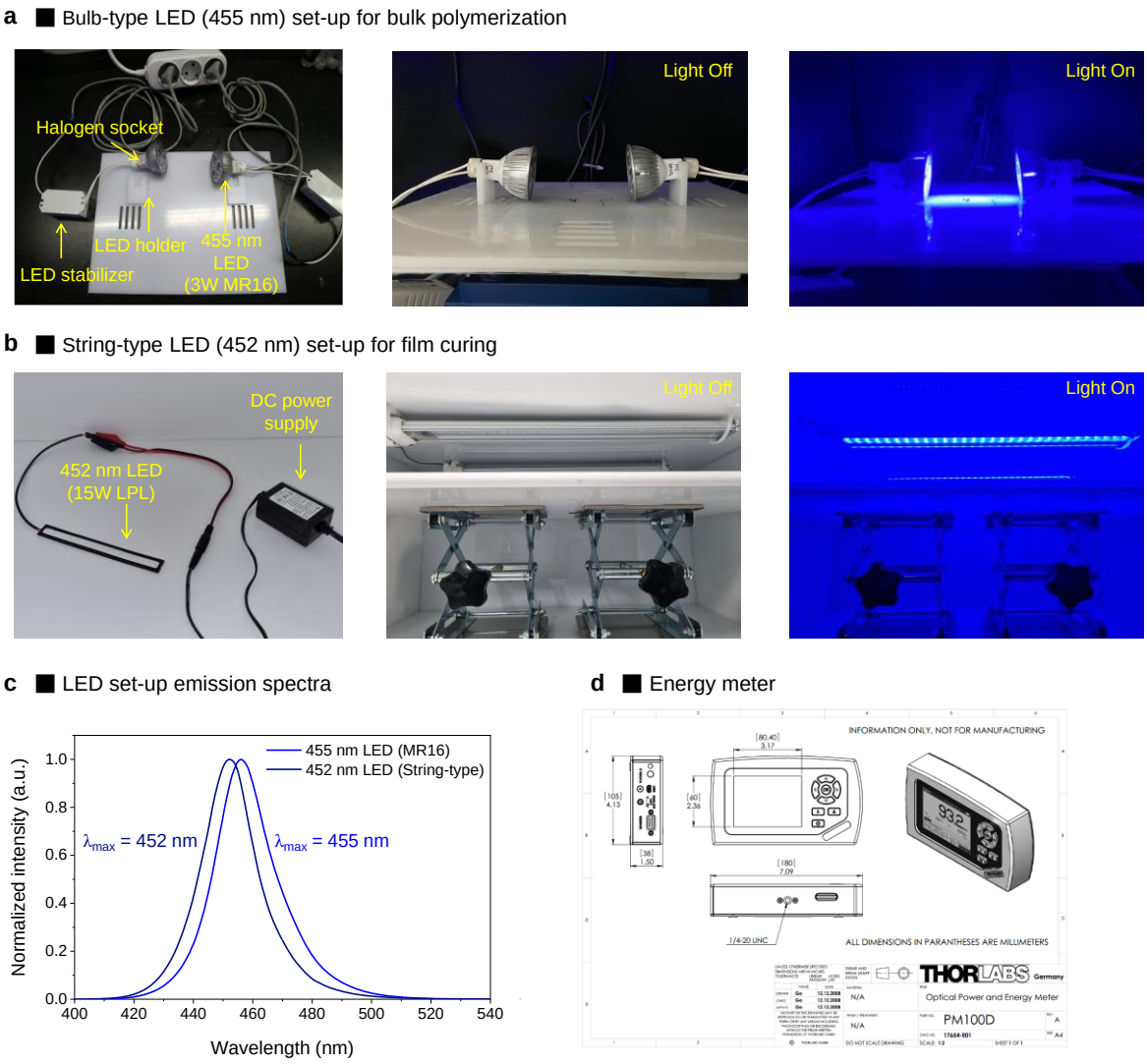

*Experimental set-up for bulk polymerization and film curing. Blue LEDs set-up for **a** bulk polymerization for the synthesis of acrylic syrup and **b** film curing. **c** LED set-up emission spectra. **d** Energy meter for evaluation of light intensity.*

■ Photophysical measurements

UV/vis spectrophotometer at RT were measured with a V-770 (JASCO) UV-Vis-NIR spectrometer equipped with a halogen lamp and photomultiplier tube (PMT) for a correction in UV/vis region. Steady-state PL emission spectra at RT were obtained with QuantaMaster 40 (Photon Technology International) UV/vis steady state spectrofluorometer equipped with a 75W Xe short arc lamp; the emission spectra were corrected for the sensitivity of the PMT. Low-temperature steady-state PL spectra was measured with a FP-8300 (JASCO) spectrofluorometer and their gated low-temperature gated PL spectra were acquired with a delay of 100 ms. PL decay measurements were carried out by the time-correlated single photon counting (TCSPC) technique. The excitation source was a 377 nm pulsed diode laser (LDH series PicoQuant) of pulse width (FWHM) < 49 ps. A NanoHarp−250 TCSPC event timer with 64 ns (for 4DP-IPN) or 8 ns (4Cz-IPN) time resolution was employed to measure decays of delayed fluorescence. The decay time fitting procedure was carried out by using the Fluofit software (PicoQuant).

■ Electrochemical measurements

Cyclic voltammetry (CV) experiments were carried out with a VersaSTAT3-200 (Princeton Applied Research) using a one compartment electrolysis cell consisting of a glassy carbon working electrode, a platinum wire counter electrode, and a quasi Ag+/Ag (sat. KCl aqueous solution) reference electrode bought from AT FRONTIER (Part No. R303). Specifically, the electrode is a silver wire that is coated with a thin layer of silver chloride and an insulated lead wire connects the silver wire with measuring instrument. The electrode also consists of a porous plug on the one end which will allow contact between the field environment with the silver chloride electrolyte. Saturated potassium chloride is added inside the body of the electrode to stabilize the silver chloride concentration and in this condition the electrode's reference potential is known to be +0.197 V at 25 ℃. The measurements were done in 0.2 mM CH_3CN solution with 0.1 M tetrabutylammonium hexafluorophosphate ($n\text{-}Bu_4NPF_6$, Aldrich, Electrochemical grade) as supporting electrolyte at a scan rate of 100 mV/s. The redox potential was calibrated after each experiment against the ferrocenium/ferrocene couple (Fc^+/Fc), which allowed conversion of all potentials to the aqueous saturated calomel electrode (SCE) scaled by using E^0 (Fc^+/Fc) = 0.42 V vs SCE in CH_3CN.[4] The working solution was degassed with 99.9999% argon for 15 min before measurement and then kept under a positive argon pressure during the measurement.

■ Fourier-transform infrared (FT-IR) spectroscopy measurements

FT-IR spectroscopy was performed with Nicolet iS50 (Thermo Fisher Scientific) coupled with four position source mirror (polaris long-lifetime mid-IR source, tungsten-halogen NIR/Vis source, raman InGaAs detector, focused emission port), three position detector mirror (LN_2 cooled, DLaTGS, RT), and attenuated total reflectance (ATR, iS50, all-reflective diamond ATR, mid- to far-IR capable: 80 to over 5000 cm^{-1}, pressure applied to 60 lbs). Conversion of acrylic syrup and film was measured ATR mode, and scan number was set as n = 16. For FT-IR specimens, the prepared acrylic syrup and film were stored in aluminum foil and measured without any post-treatment.

■ Gel permeation chromatography (GPC) measurements

Molecular weight was measured with GPC (Waters system; Waters 1515 isocratic pump, Waters 2707 autosampler) coupled with refractive index (RI) detector (Waters 2414 RI detector), UV/vis detector (Waters 2489 UV/vis detector), Gel permeation chromatography-multi-angle laser light scattering (GPC-MALS, Wyatt DAWN 8) and three different columns (Agilent Polypore 300 × 7.5 mm, Jordi mixed bed 300 × 8.0 mm, Waters Styragel HR4 300 × 7.8 mm).

■ Universal testing machine (UTM) measurements

Peel strength was performed with LS1 (AMETEK, USA). A load cell with a capacity of 10 kgf was used, and the test specimens were fixed by clamp used for a tensile test. For the peel test specimens, the acrylic syrup is cured between PETE film and release films, and the cured specimen is cut to 1 cm wide. The release film was removed from the specimen, and the adhesive film was attached to the adherend using a 2 kg roller (2 round trips over the film). The peel strength was measured after 24 h of attachment. Glass and CPI were used as adherents.

■ Dynamic mechanical analysis (DMA) measurements

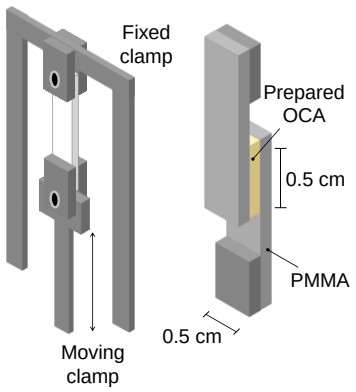

Experimental setup for DMA

Viscoelastic properties including strain recovery, stress relaxation and maximum stress were evaluated with Q800 (TA instrument). Film tension clamp used for evaluation of soft materials such as rubber was employed.[5] Specimen for DMA was prepared by laminating the adhesive to a thickness of 50–100 μm and then cutting to a certain size (1 cm × 0.5 cm). After that, specimen was prepared by bonding between PMMA substrates. The measurements were carried out at 25 ℃, and after pulling the specimen with 300% strain for 10 min, it was recovered for 5 min.

■ Dynamic folding test measurements

Folding durability was evaluated with Foldy-200 (FlexiGO, Republic of Korea) coupled with an inspection system capable of micro vision, macro vision, display inspection, and surface profiling. The samples were prepared by stacking colorless polyimide (CPI, PI Advanced Materials, 50 μm), prepared OCA (50 μm), yellow PI (GL140A, 35 μm), CEF 3602 (3M, 50 μm), and yellow PI (GL140A, 35 μm) in this order (see Supplementary Fig. 18). The samples were measured with a fixed radius of curvature of 1.5 mm along with folding cycles as 0.5 Hz by 5 x 10^4 times at -20 ℃.

■ Rheometer measurements

Storage modulus (G'), loss modulus (G''), and damping factor (tan δ) were evaluated with Discovery HR-3 (TA instrument) coupled with optical encoder dual reader, 2nd generation magnetic thrust bearing (Patent US # 7,137, 290 & 7,017,393), advanced drag cup motor (Patent US # 6,798,099), normal force rebalance transducer, new true position sensor (TPS), and active temperature control (ATC, Patent US # 6,931,915). Specimen for rheometer was prepared by laminating the PSAs to thickness of 0.8–1 mm and then cutting to certain size (8 mm in diameter.). The measurements were carried out at 25–85 ℃, 1 Hz 0.5% shear.

■ Gel content measurements

The fraction of crosslinked polymers was evaluated by gel content measurement. Approximately 0.5 g of OCA sample was dissolved in 35 ml toluene at RT for 24 h, then linear polymers were completely dissolved, whereas the crosslinked polymers were swelled. The crosslinked polymers were isolated by filtration using a steel mesh (#200, ~74 μm). After the filtration, the sample was dried under reduced pressure at 80 ℃ for 24 h. Gel content was calculated by following equation.

$$\text{Gel content (\%)} = \frac{W_{\text{filtered OCA}}}{W_{\text{initial OCA}}} \times 100$$

where $W_{\text{filtered OCA}}$ and $W_{\text{initial OCA}}$ mean weight of the crosslinked polymers filtered over mesh and weight of OCA samples that initially dissolved in toluene.

■ Preparation of organic light-emitting diode (OLED)

We fabricated bottom-emitting, blue fluorescent OLEDs through a thermal evaporation process carried out under a base pressure of 3 x 10^{-7} Torr. The device structure is as follows: 70 nm indium tin oxide as an anode, 5 nm hole-injection layer (HIL), 25 nm hole transport layer (HTL), 60 nm emission layer (EML), 30 nm electron transport layer (ETL), 1 nm electron injection layer (EIL) and 100 nm aluminum as a cathode. All the organic compounds used to construct these blue OLEDs were sourced from SFC Co., Ltd. The OLEDs had dimensions of 2 mm x 2 mm, defined as the overlapping area between the cathode and anode. To minimize the undesirable effects of environmental defects, all devices were encapsulated within a N_2 atmosphere, with O_2 and moisture concentrations maintained below 1 ppm. The OCA film was directly applied on to one side of the glass substrate where devices were not present. The OCA film serves the dual purpose of extracting photons emitted by OLEDs and allowing external UV light to penetrate through it and illuminate the OLEDs. In case of the OCA film with UVA, UV light can be effectively blocked, as detailed in the main text.

■ UV-blocking test of OLEDs covered by OCAs

Both an OLED covered by non-UV-blocking OCA and the same device with UV-blocking OCA underwent simultaneous illumination using a UV light-emitting diode (LED) source (Kessil, PR160L) with a peak wavelength of λ_{max} = 368 nm and an intensity of 70 mW/cm^2 at room temperature. Both devices were consistently operated under a constant current density of J = 25–100 mA/cm^2, utilizing a multi-channel source measure unit (Agilent Technologies, U2722A). During the measurement of luminance levels over time with a 10 min interval, we momentarily deactivated the UV LED for 5 s to prevent the detection of photoluminescent signals originating from the OLEDs due to UV irradiation. Upon turning off the UV LED, a waiting period of 3 s was observed, followed by a 2 s measurement of electroluminescence from the OLEDs. This measurement involved the averaging of 20 collected signals, each spaced at 0.1 s intervals, in order to minimize detection errors. Degradation of OLEDs' luminance over time was captured using a photodiode (Thorlabs, SM1PD1A) and subsequently recorded through a data logger (Keysight, DAQ970A). All stages of OLED testing were fully automated through an in-house LabVIEW virtual instruments.

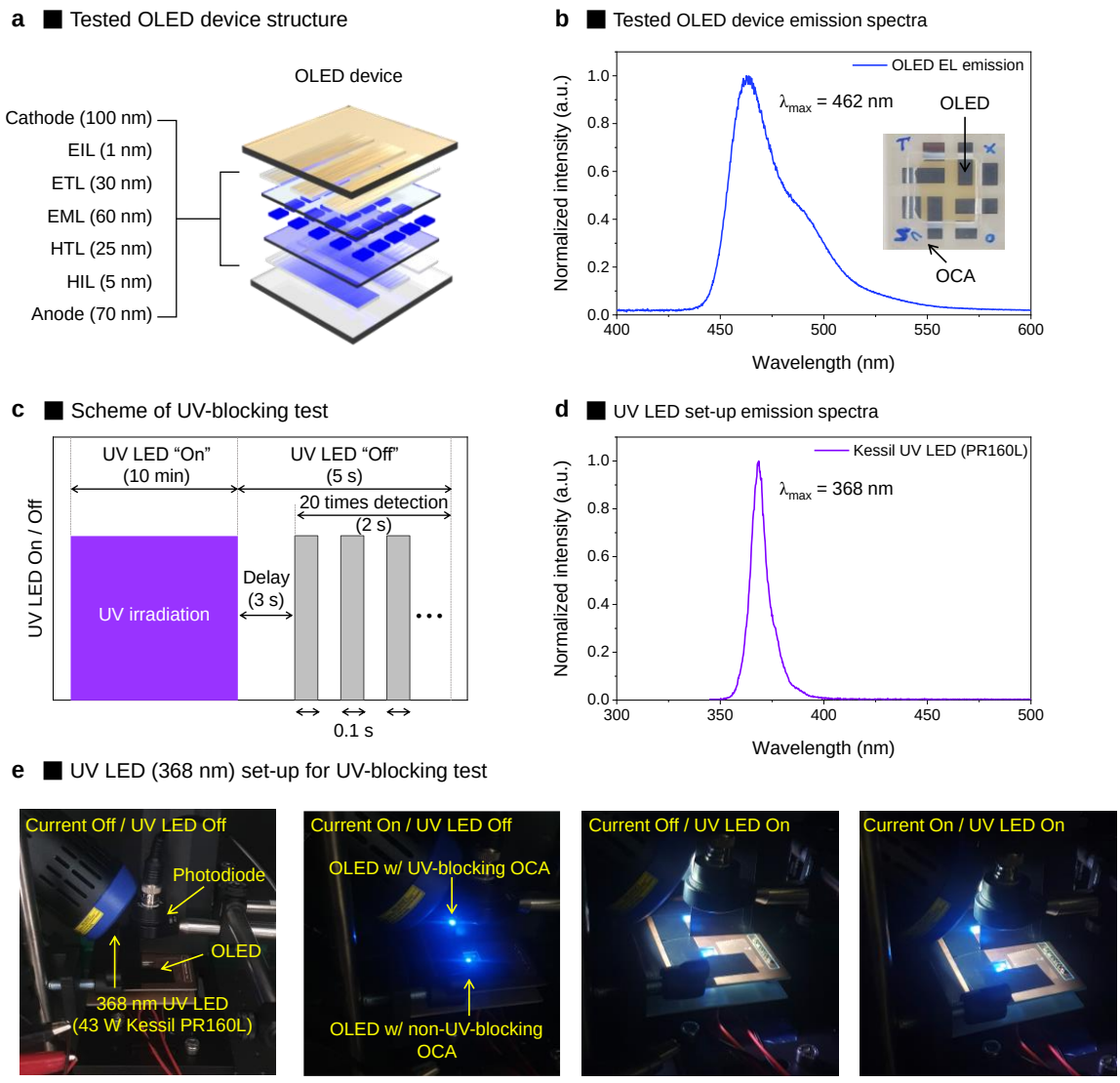

a *Structure of OLED devices tested in UV-blocking test.* ***b*** *Electroluminescence (EL) emission spectra of tested OLED devices.* ***c*** *Scheme of UV-blocking test of OCAs.* ***d*** *UV LED emission spectra used in UV-blocking test setup.* ***d*** *Experimental set-up for UV-blocking test.*

1.4. Computational methods

■ Time-dependent density functional theory (TD-DFT) and kinetic simulation

Density functional theory (DFT) and time-dependent (TD) DFT calculations were performed with the B3LYP functional and 6–311++G* basis set as all implemented in the Gaussian16 program package. The geometries optimization, single point energies and oscillator strengths of vertical transition were calculated in ethyl acetate solution employing the polarizable continuum model (PCM). In all geometry optimization calculations, the frequency calculations were performed both to verify that the geometries were true minima. To obtain the calculated excited state energy of PCs and UVAs, vertical transition energies for S_1 and T_1 were obtained by single-point calculations on the optimized S_0 geometries, respectively. The frontier molecular orbitals (MOs) were drawn by GaussView 6.0 software.

Kinetic simulation were performed with the ordinary differential equations (ODE) based on the rate law using ODE 15s or ODE 23s solvers implemented in the Matlab program package.[2,6] The concentration of S_1 and T_1 can be described by following system of ordinary differential equations (ODE).

$$\frac{d[S_1]}{dt} = k_{RISC}[T_1] - \left(k_{ISC} + k_{r,S_1} + k_{nr,S_1}\right)[S_1] \quad (1)$$

$$\frac{d[T_1]}{dt} = k_{\mathrm{ISC}}[S_1] - (k_{\mathrm{RISC}} + k_{\mathrm{r,T_1}} + k_{\mathrm{nr,T_1}})[T_1] \quad (2)$$

where k_{ISC}, k_{RISC}, $k_{\mathrm{r,S1}}$, $k_{\mathrm{r,T1}}$, $k_{\mathrm{nr,S1}}$ and $k_{\mathrm{nr,T1}}$ denote the rate constants of intersystem crossing, reverse-intersystem crossing, radiative decay from S_1, radiative decay from T_1, non-radiative decay from S_1, and non-radiative decay from T_1, respectively. These coupled nonlinear rate equations enable to trace time-dependent decay of the S_1 and T_1 state generated by single pulsed-photoexcitation (see Supplementary Note 2.3 for the more detail).

Supplementary Note 2. Characterization of PC, co-initiator and UVA

2.1. Syntheses of PCs and UVA-1

■ Synthesis of 4DP-IPN

A solution of NaH (60% in mineral oil, 0.477 g, 11.94 mmol) and diphenylamine (1.48 g, 8.75 mmol) in anhydrous DMAc (5 ml) was stirred for 30 min in ice bath under a nitrogen atmosphere. After 30 min, 2,4,5,6-tetrafluoroisophthalonitrile (0.4 g, 1.99 mmol) dissolved in DMAc (5 ml) was slowly added to the reaction mixture and stirred further at 100 ℃ for 10 h. Afterwards, distilled water (2 ml) was poured into the reaction mixture to quench the excess NaH and, methanol was added to precipitate the crude product, which was further purified by column chromatography on silica gel (CH_2Cl_2:hexanes, 2:3 v/v) to give pure product as yellow powder (1.32 g, 83%). ^{1}H NMR data in full agreement with those reported in literature.[1,2] ^{1}H NMR (400 MHz, DMSO-d_6): δ 7.31–7.21 (m, 8H), 7.10–7.05 (t, 8H), 7.03–6.97 (t. 2H), 6.91–6.75 (m, 16H), 6.68–6.62 (m, 6H).

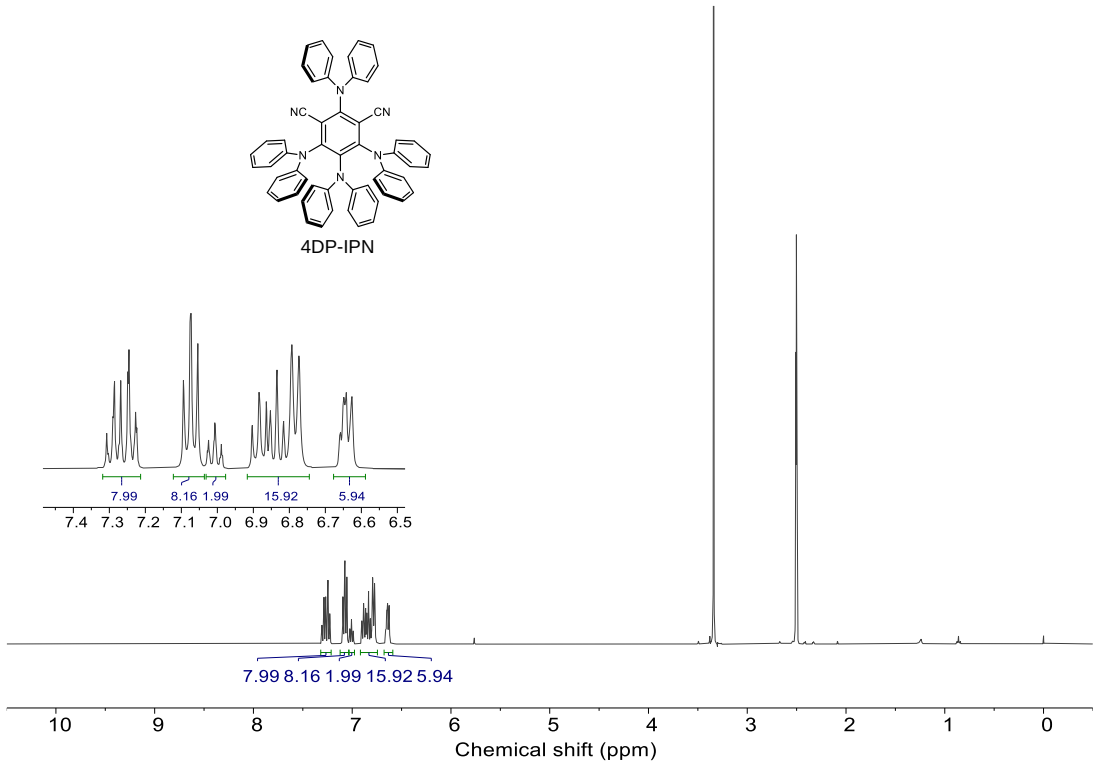

^{1}H NMR data of 4DP-IPN at RT (400 MHz, DMSO-d_6). ^{1}H NMR (400 MHz, DMSO-d_6): δ 7.31–7.21 (m, 8H), 7.10–7.05 (t, 8H), 7.03–6.97 (t. 2H), 6.91–6.75 (m, 16H), 6.68–6.62 (m, 6H).

■ Synthesis of 4Cz-IPN

A solution of t-BuOK (0.193 g, 1.72 mmol) and 3,6-di-tert-butyl-9H-carbazole (0.400 g, 1.43 mmol) in anhydrous THF (40 ml) was stirred for 30 min in ice bath under a nitrogen atmosphere. After, 2,4,5,6-tetrafluoroisophthalonitrile (0.057 g, 0.28 mmol) was slowly added to the reaction mixture and stirred further for 12 h. After completion of the reaction, distilled water (2 ml) was poured into the reaction mixture to quench the excess t-BuOK. The resulting solution was concentrated under reduced pressure followed by washing several times with water and ethanol to yield the crude product, which was purified by column chromatography on silica gel (CH_2Cl_2:hexane, 2:1 v/v) to give pure product as pale yellow powder (0.160 g, 45%). ^{1}H NMR data in full agreement with those reported in literature.[1,2] ^{1}H NMR (400 MHz, $CDCl_3$): δ 8.21 (d, 2H), 7.74 (dd, 2H), 7.61–7.59 (m, 6H), 7.18 (d, 2H), 7.05–7.00 (m, 8H), 6.51 (dd, 2H), 6.44 (d, 2H), 1.53 (s, 18H), 1.30 (s, 36H), 1.22 (s, 18H).

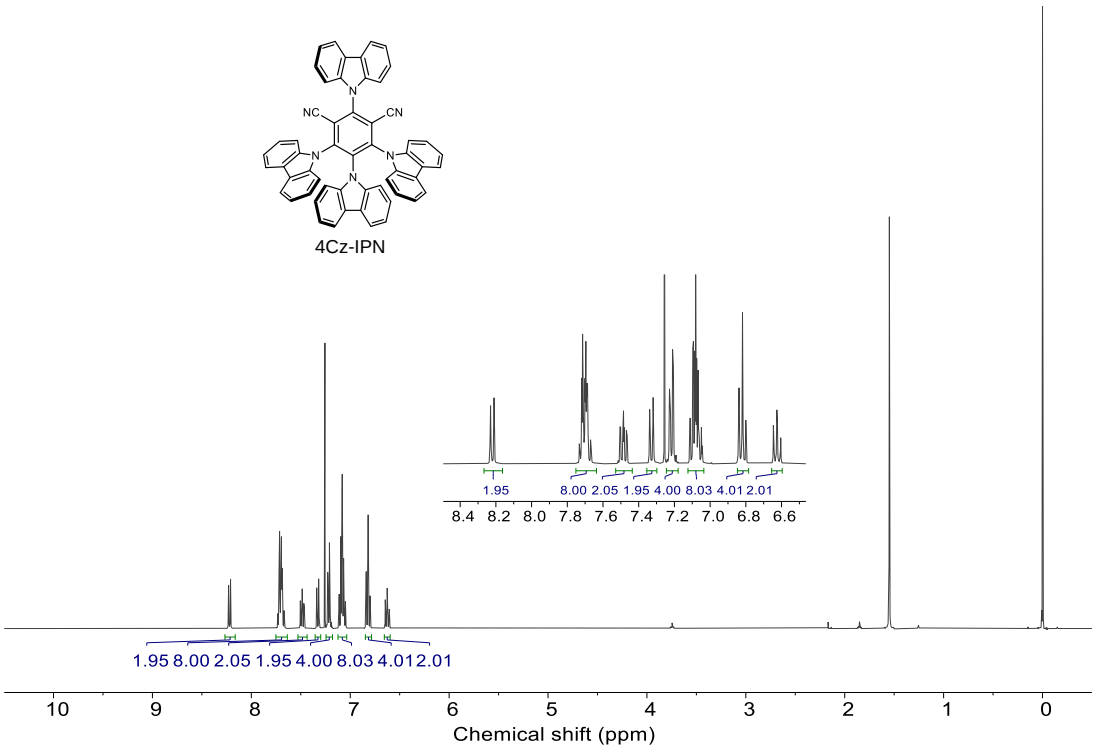

^{1}H NMR data of 4Cz-IPN at RT (400 MHz, $CDCl_3$). ^{1}H NMR (400 MHz, $CDCl_3$): δ 8.22 (dt, 2H), 7.74–7.67 (m, 8H), 7.49 (ddd, 2H), 7.33 (dt, 2H), 7.23–7.21 (m, 4H), 7.12–7.05 (m, 8H), 6.82 (td, 4H), 6.63 (ddd, 2H).

■ Synthesis of UVA-1

4-(dimethylamino)benzaldehyde (5.00 g, 33.51 mmol) and dimethyl malonate (4.87 g, 36.86 mmol) were dissolved in methanol (50 ml). Then, DBU (1,8-diazabicyclo[5.4.0]undec-7-ene, 0.45 mL, 3.01 mmol) was added into the solution. The mixture was stirred at RT for 24 h. The solvent was partially removed under reduced pressure and the solution was poured into distilled water (100 ml). The generated precipitate was filtered and washed with water and methanol. After drying under reduced pressure, 7.54 g of dimethyl 2-(4-(dimethylamino)benzylidene)malonate) was obtained as yellow powder (yield: 85.48%). ^{1}H NMR data in full agreement with those reported in literature.[3] ^{1}H NMR (400 MHz, $CDCl_3$): δ 7.67 (s, 1H), 7.36–7.29 (m, 2H), 6.67–6.60 (m, 2H), 3.88 (d, 3H), 3.81 (d, 3H), 3.03 (d, 6H).

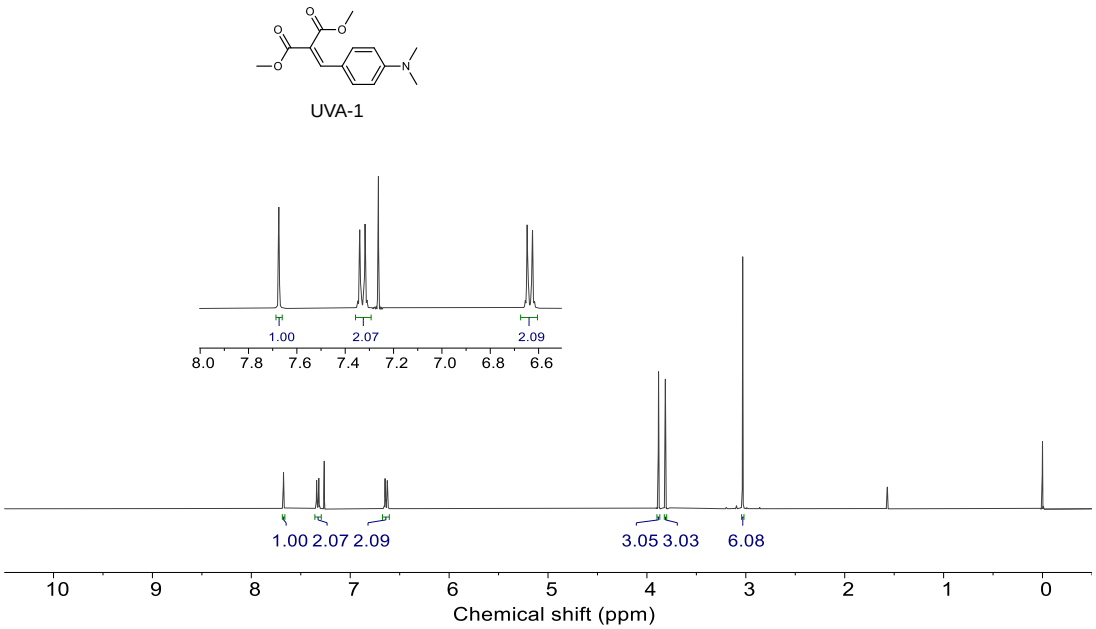

^{1}H NMR data of UVA-1 at RT (400 MHz, $CDCl_3$). ^{1}H NMR (400 MHz, $CDCl_3$): δ 7.67 (s, 1H), 7.36–7.29 (m, 2H), 6.67–6.60 (m, 2H), 3.88 (d, 3H), 3.81 (d, 3H), 3.03 (d, 6H).

2.2. Characterization of PC, co-initiator and UVA

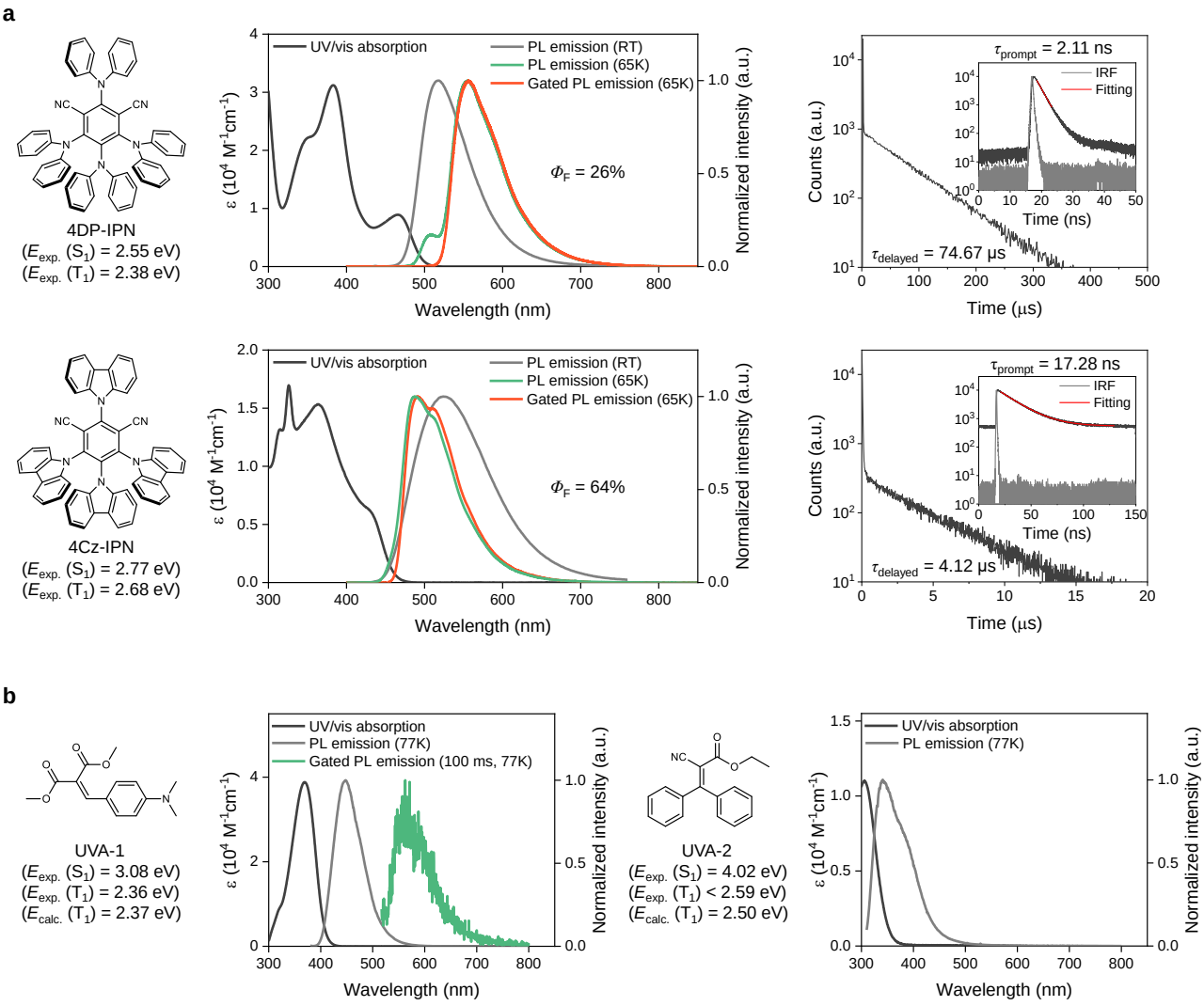

Supplementary Fig. 1 Chemical structures and photophysical properties of **a** PCs and **b** UVAs including UV/vis absorption and photoluminescence (PL) emission spectra in ethyl acetate acetate (1.0×10^{-5} M).[3] Delayed fluorescence decay spectra of PCs were obtained at RT after the degassing process by purging with 99.9999% argon for 10 min, however, prompt PL decay were obtained without degassing process. E (S_1) and E (T_1) were extracted from the onset of PL and onset of gated PL in ethyl acetate at 65 K, respectively. The onsets were obtained by tangential method; i.e., the intersection of the tangent, set at the high energy slope of the spectrum, with the x-axis. Because the phosphorescence of UVA-2 was not observed,[7] therefore E (T_1) of UVA-2 was referred to the literature, where E (T_1) was estimated from the phosphorescence quenching experiments with the quencher,[7] having E (T_1) = 2.59 eV re-estimated in this work with onset of gated PL in ethanol at 77 K. E (T_1) of UVAs calculated by TD-DFT were also given.

Supplementary Table 1 Photophysical properties of PCs in ethyl acetate.[3] The photophysical rate constants were derived by experimental and computational methods in this work followed by the procedure that our group studied.[2,3]

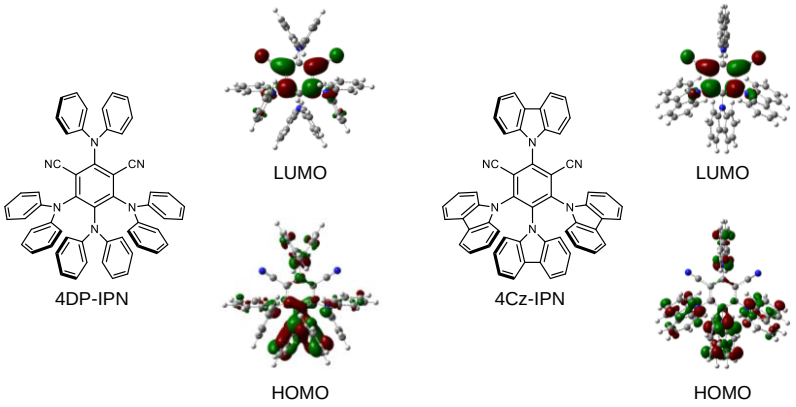

PC	E (S_1) (eV) [a]	E (T_1) (eV) [b]	τ_{prompt} (ns)	$\tau_{delayed}$ (μs)	$\lambda_{max,abs}$ (nm)	$\lambda_{max,em}$ (nm)	$f_{S0\rightarrow S1}$ [c]	Φ_F	Φ_{ISC}	$k_{r,S1}$ (10^7 s^{-1})	$k_{nr,S1}$ (10^7 s^{-1})	k_{ISC} (10^8 s^{-1})	$k_{r,T1}$ (s^{-1})	$k_{nr,T1}$ (s^{-1})	k_{RISC} (10^5 s^{-1})
4DP-IPN	2.55	2.38	2.11	74.67	465	518	0.0750	0.26	0.75	3.1	8.9	3.5	-	-	0.55
4Cz-IPN	2.77	2.68	17.28	4.12	422	524	0.0742	0.64	0.26	2.7	1.5	0.15	-	-	3.3

E_{00} were extracted from the [a]onset of PL and [b]onset of gated PL in ethyl acetate at 65 K, respectively. The onsets were obtained by tangential method; i.e., the intersection of the tangent, set at the high energy slope of the spectrum, with the x-axis. [c]Oscillator strengths were obtained by TD-DFT calculation.

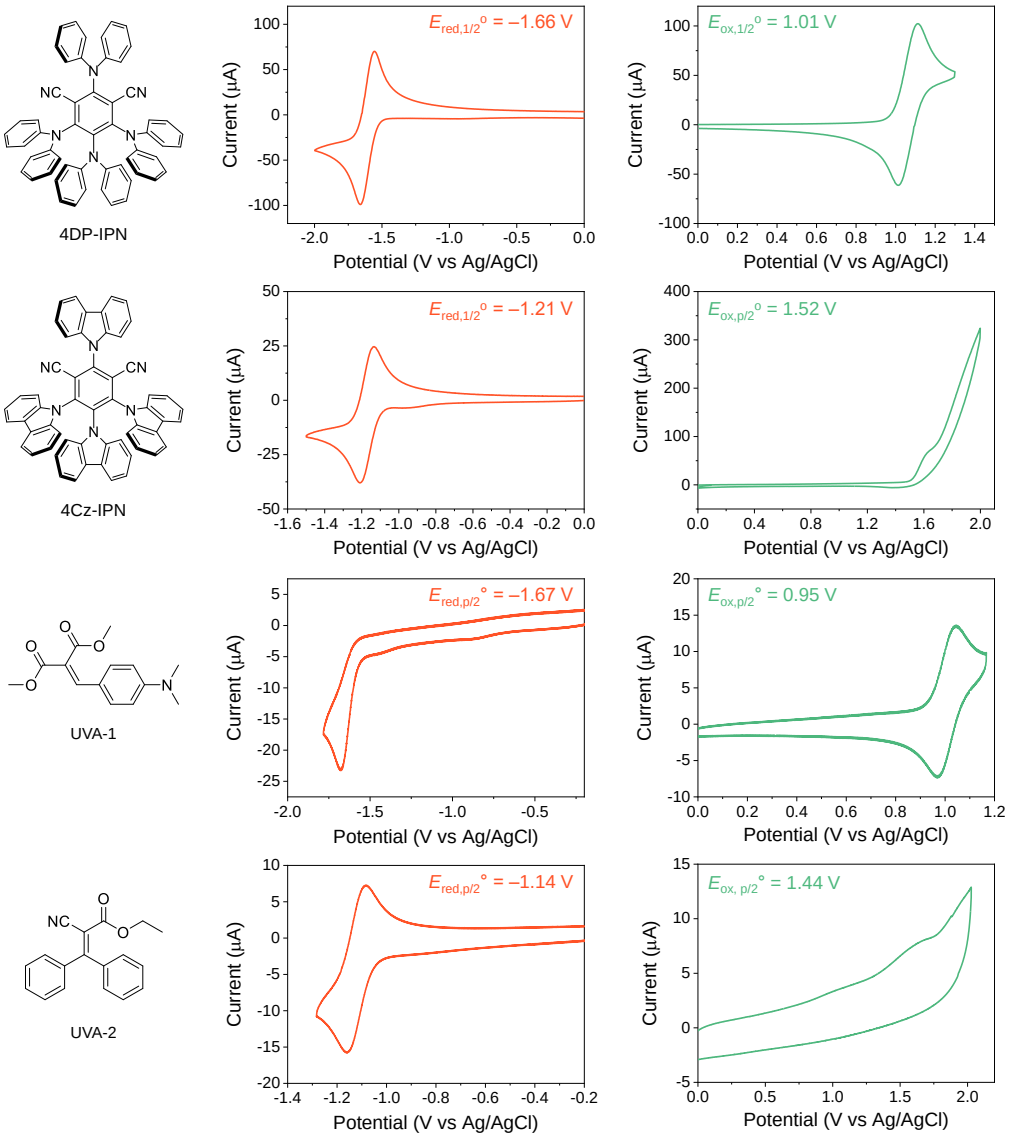

Supplementary Fig. 2 Chemical structures and CV spectra of PCs and UVAs studied in this work. CV spectra were obtained in CH_3CN (2.0×10^{-4} M) at RT after the degassing process by purging with 99.9999% argon for 15 min. For reversible CV cycle, the potentials were evaluated as their half-potentials ($E_{1/2}^{0}$), however, for irreversible CV cycle, the potentials were obtained from their half-peak potentials ($E_{p/2}^{0}$).[4] All potentials were converted to the SCE scale by using E^0 (Fc^+/Fc) = 0.42 V vs SCE in CH_3CN.[4]

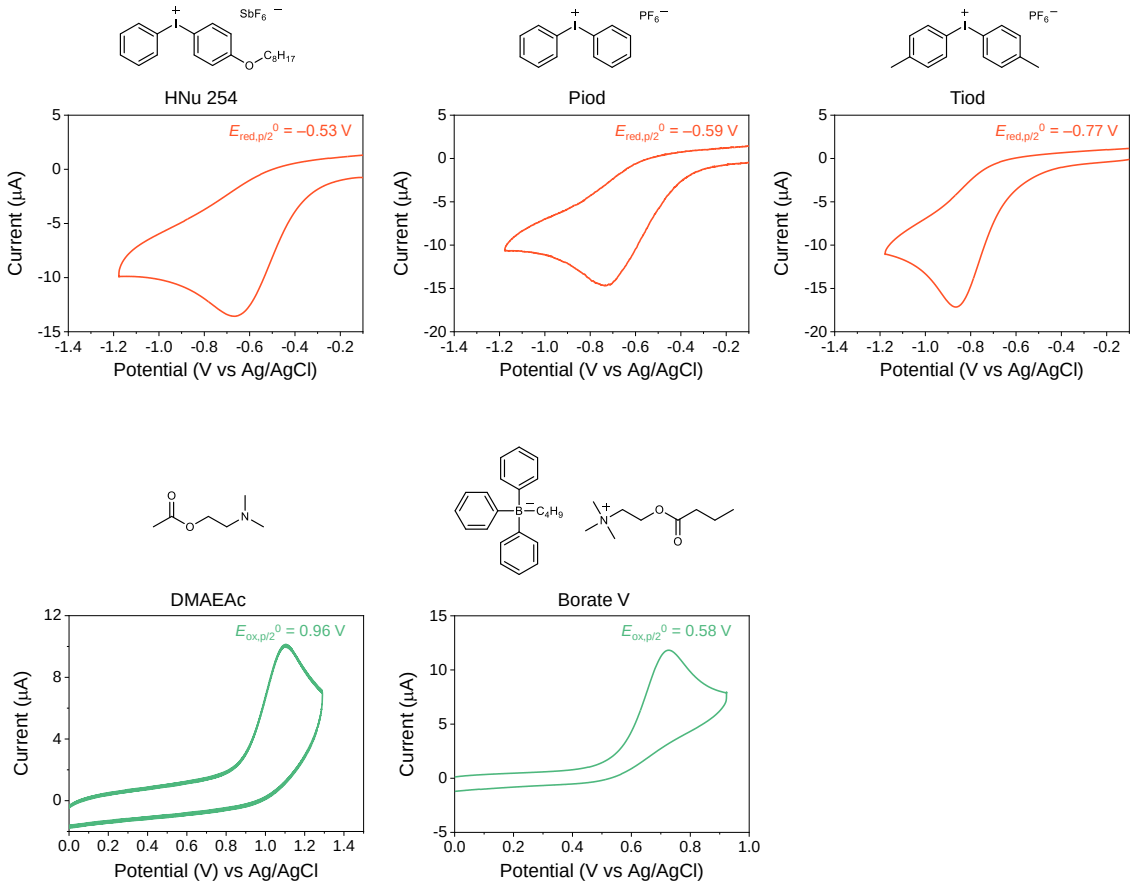

Supplementary Fig. 3 Chemical structures and CV spectra of co-initiators studied in this work. CV spectra were obtained in CH_3CN (2.0×10^{-4} M) at RT after the degassing process by purging with 99.9999% argon for 15 min. For irreversible CV cycle, the potentials were obtained from their half-peak potentials ($E_{p/2}^0$).[4] All potentials were converted to the SCE scale by using E^0 (Fc^+/Fc) = 0.42 V vs SCE in CH_3CN.[4]

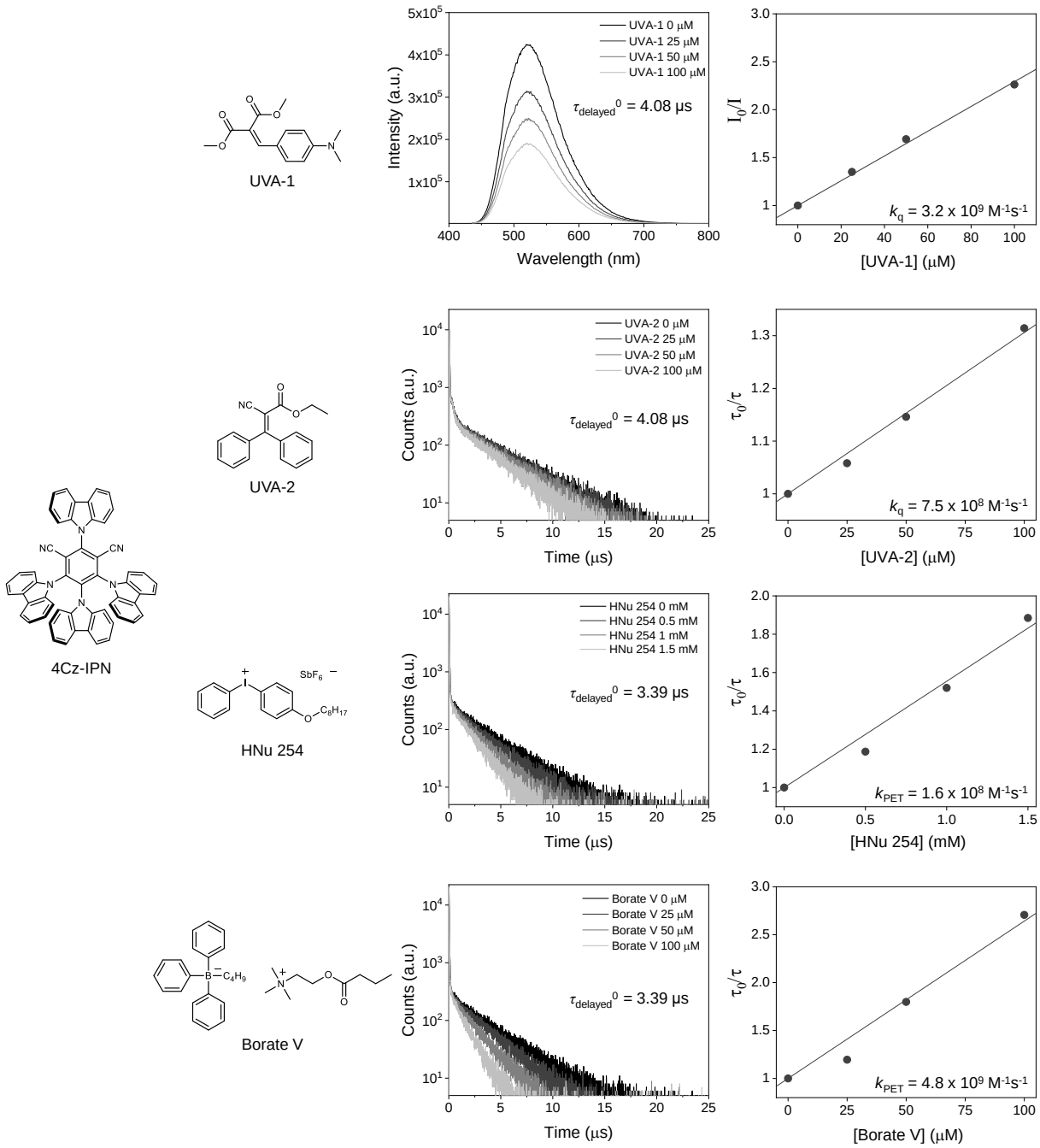

Supplementary Fig. 4 Chemical structures and Stern-Volmer plots of PL quenching of 4Cz-IPN at RT along with addition of UVAs and co-initiators; here PET denote photoinduced electron transfer. Generally, delayed fluorescence decay at RT spectra were taken from the degassed solutions of 4Cz-IPN in ethyl acetate (1.0×10^{-5} M) varying the concentration of quenchers. Generally, PL quenching experiments were conducted by measurement of the change of PL decay with time-correlated single photon counting (TCSPC) techniques monitored at λ_{ex} = 377 nm and λ_{det} = 520 nm. PL quenching experiments with UVA-1 were conducted by measurement of the change in intensity maxima of steady-state PL emission at λ_{ex} = 420 nm.

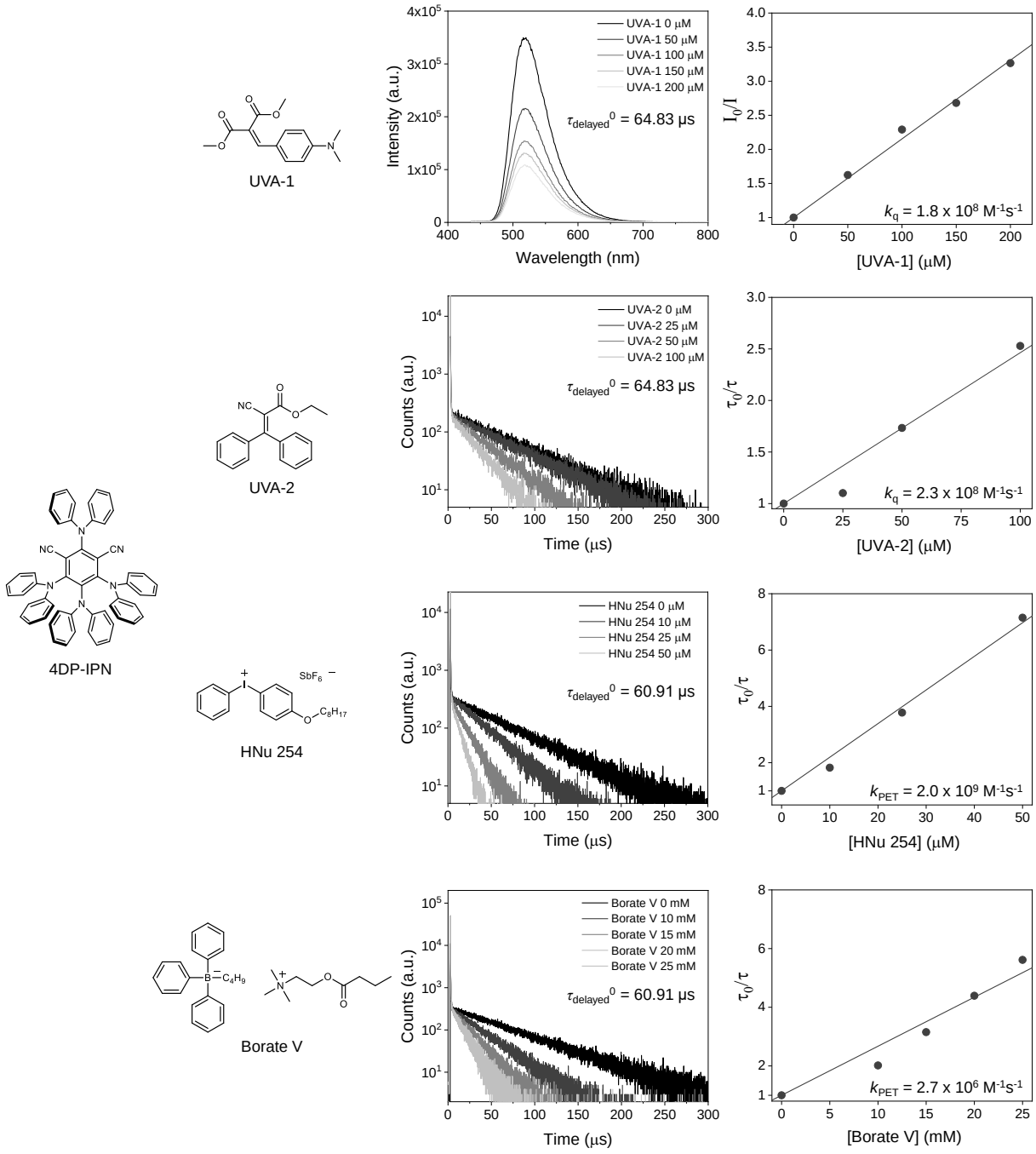

Supplementary Fig. 5 Chemical structures and Stern-Volmer plots of PL quenching of 4DP-IPN at RT along with addition of UVAs and co-initiators; PET denote photoinduced electron transfer. Generally, delayed fluorescence decay at RT spectra were taken from the degassed solutions of 4DP-IPN in ethyl acetate (1.0×10^{-5} M) varying the concentration of quenchers. Generally, PL quenching experiments were conducted by measurement of the change of PL decay with time-correlated single photon counting (TCSPC) techniques monitored at λ_{ex} = 377 nm and λ_{det} = 520 nm. PL quenching experiments with UVA-1 were conducted by measurement of the change in intensity maxima of steady-state PL emission at λ_{ex} = 420 nm.

Supplementary Table 2 Electronic structure of PCs and UVAs. Ionization potential (IP) and electron affinity (EA) of each species were evaluated from CV measurement in CH_3CN and DFT calculations on the optimized geometries of radical cations/anions in ethyl acetate employing B3LYP functional, 6–311++G* basis set and the polarizable continuum model (PCM).

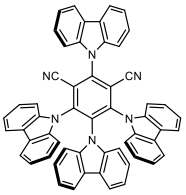

4Cz-IPN

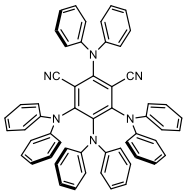

4DP-IPN

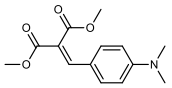

UVA-1

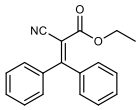

UVA-2

	IP (eV)			EA (eV)			*E* (T_1) (eV)	
	calc.[a]	calc.[b]	exp.[c]	calc.[a]	calc.[b]	exp.[c]	calc.[d]	exp.[e]
4Cz-IPN	6.05	6.04	5.90	2.98	3.26	3.17	2.34	2.68
4DP-IPN	5.61	5.57	5.39	2.56	2.71	2.72	2.21	2.38
UVA-1	5.91	5.85	5.33	2.07	2.39	2.71	2.37	2.36
UVA-2	6.87	6.83	5.82	2.72	3.04	3.24	2.50	< 2.59 [f]

a: IP and EA were computationally evaluated from energy level of HOMO and LUMO by Koopmans' theorem.
b: IP and EA were computationally evaluated from electronic energy differences between the optimized geometries of radical cations/anions and neutral state, respectively.
c: IP and EA were experimentally evaluated from CV measurements converted by IP = E_{ox}^0 (V vs SCE) + 4.8 eV - 0.42 eV and EA = E_{red}^0 (V vs SCE) + 4.8 eV - 0.42 eV, respectively. This value 4.8 eV is the HOMO energy level of ferrocene against vacuum[8] and 0.42 eV is the half-potential of ferrocene against SCE calibrated for CV measurements in this work.[4]
d: *E* (T_1) were computationally evaluated from TD-DFT for vertical transition (from S_0 to T_1) obtained by single-point calculations on the optimized geometry of neutral state.
e: *E* (T_1) were experimentally evaluated from the onset of gated PL emission spectra in ethyl acetate at low temperature (65 or 77K).
f: *E* (T_1) of UVA-2 was referred to the literature.[7]

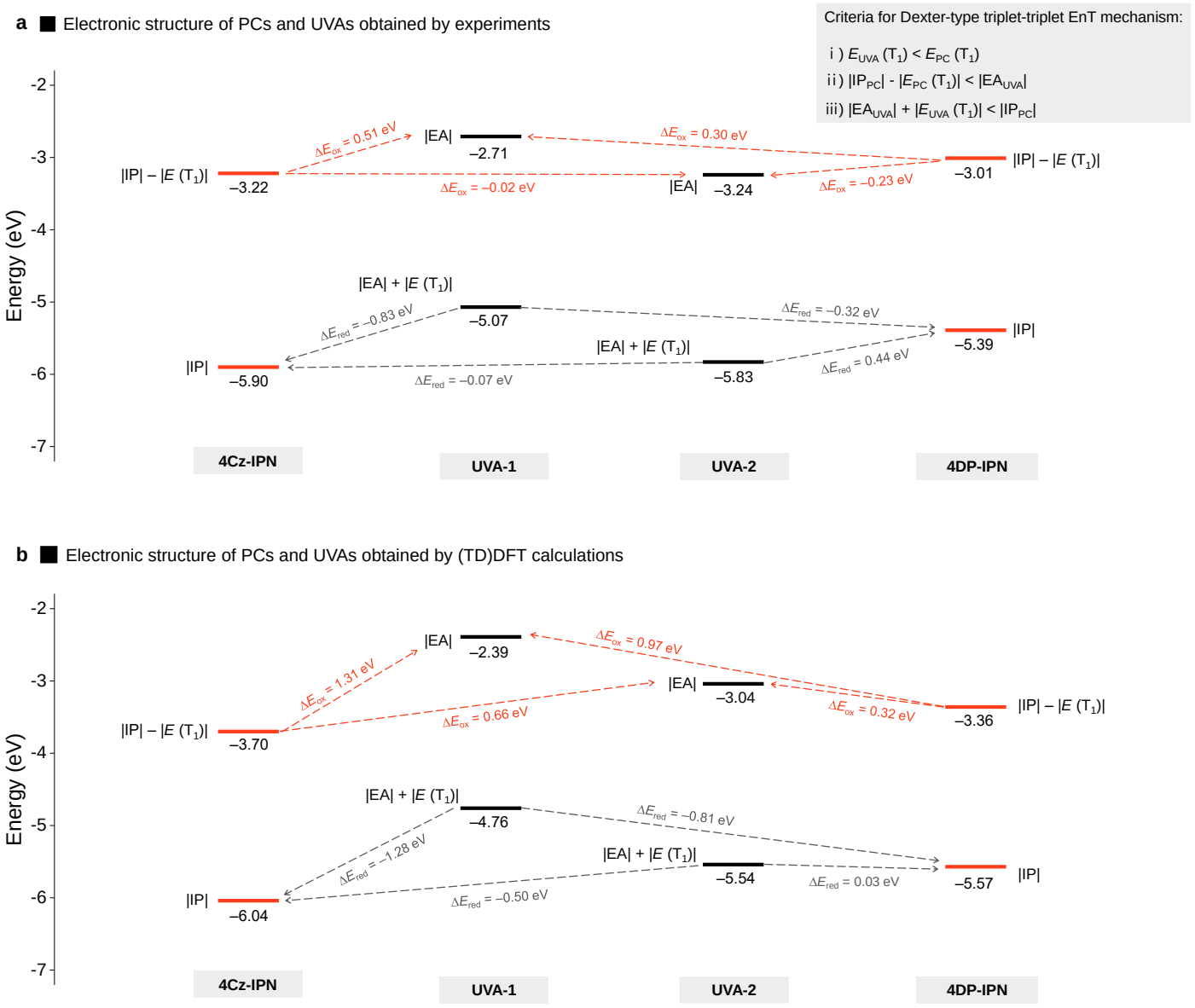

Supplementary Fig. 6 Electronic structure of PCs and UVAs obtained by **a** experiments and **b** (TD)DFT calculations. The driving forces (i.e., ΔE_{ox} and ΔE_{red}) for each step of electron exchange in Dexter-type triplet-triplet EnT between $^3PC^*$ and UVAs are given; initial electron transfer pathway (orange dashed line) and following electron transfer pathway (black dashed line). The energy values (i.e., IP, EA and E (T_1)) obtained by experiments (i.e. CV measurement and onset of gated PL emission at low temperature) and (TD)DFT calculations are listed in Supplementary Table 2.

Supplementary Table 3 Experimental evaluation of driving forces for photoinduced electron transfer between PCs and UVAs. It is notable that errors from experimental or computational method are inherent and these inaccuracies can be up to 0.5 eV making our evaluation over-/underestimated.

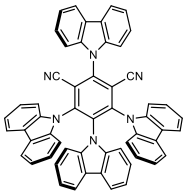

4Cz-IPN

$E_{ox,\,exp.}{}^{*}$ (S_1) = –1.25 V $E_{ox,\,exp.}{}^{*}$ (T_1) = –1.16 V
$E_{red,\,exp.}{}^{*}$ (S_1) = 1.56 V $E_{red,\,exp.}{}^{*}$ (T_1) = 1.47 V

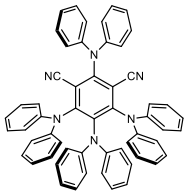

4DP-IPN

$E_{ox,\,exp.}{}^{*}$ (S_1) = –1.54 V $E_{ox,\,exp.}{}^{*}$ (T_1) = –1.37 V
$E_{red,\,exp.}{}^{*}$ (S_1) = 0.89 V $E_{red,\,exp.}{}^{*}$ (T_1) = 0.72 V

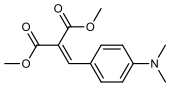

UVA-1

$E_{ox}{}^{0}$ = 0.95 V
$E_{red}{}^{0}$ = –1.67 V

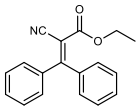

UVA-2

$E_{ox}{}^{0}$ = 1.44 V
$E_{red}{}^{0}$ = –1.14 V

–ΔG (eV)		Oxidative quenching		Reductive quenching	
PC	UVA	from $^{1}PC^{*}$	from $^{3}PC^{*}$	to $^{1}PC^{*}$	to $^{3}PC^{*}$
4Cz-IPN	UVA-1	–0.42	–0.51	0.61	0.52
	UVA-2	0.11	0.02	0.12	0.03
4DP-IPN	UVA-1	–0.13	–0.30	–0.06	–0.23
	UVA-2	0.40	0.23	–0.55	–0.72

2.3. Computational characterization of PIS: kinetic simulation

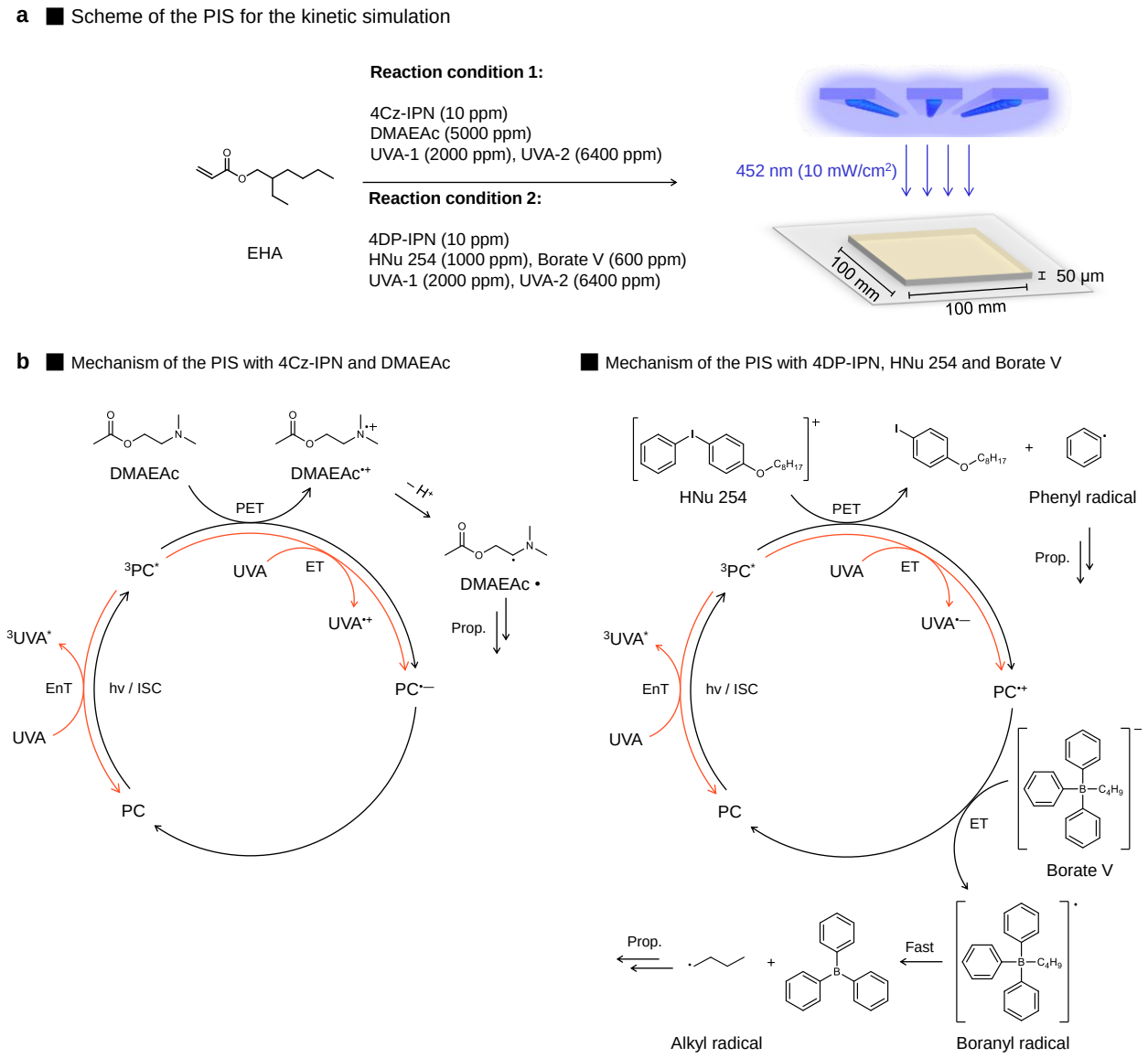

Supplementary Fig. 7 Kinetic simulation of visible-driven PIS. **a** Scheme of the PIS for the kinetic simulation. **b** Two proposed PIS mechanisms for the simplified kinetic simulation.

Kinetic simulations for the polymerization of EHA were performed based on the rate law (Supplementary Table 4 and 5). To simplify the kinetic simulation, we involved the following assumptions; 1) internal conversion (IC) is fast compared to our time scale of interest, 2) side-reactions such as triplet-triplet annihilation and photodegradation of PC are not involved, 3) no back-electron transfer (BET) is involved because spin-flipping is forbidden where $^3PC^*$ are involved,[9] 4) as the quantitative analysis of the EnT/ET processes with UVAs is challenging, to be simplified, triplet-triplet EnT with UVAs was considered as a primary quenching pathway of $^3PC^*$, 5) oxygen species (e.g., $^{1/3}O_2$ and $O_2^{\bullet-}$) are not involved, and 6) in the kinetic simulation of 4Cz-IPN and DMAEAc, there is no reaction to close the photocatalytic cycle, nevertheless there is no significant error as the only tiny amount of 4Cz-IPN and DMAEAc are consumed at initial kinetics (< 100 ms). For the photocatalytic cycle of 4DP-IPN, although both oxidative and reductive quenching cycle are involved in the kinetic simulation, but only the oxidative quenching cycle are described in Supplementary Fig. 7 as it mainly attributes to PIS.

Supplementary Table 4 Kinetic equations for all species in visible-light driven PIS.

Species	Mass balance equations
PC (S_0)	$\frac{d[S_0]}{dt} = -k_{abs}\left(1 - 10^{-\varepsilon \times l \times [S_0]}\right) + \left(k_{r,S_1} + k_{nr,S_1}\right)[S_1] + k_{ET,1}[DC][\text{Borate V}] + k_{ET,2}[DA][\text{HNu 254}] + k_{q,1}[T_1][UVA1] + k_{q,2}[T_1][UVA2]$
$^1PC^*$ (S_1)	$\frac{d[S_1]}{dt} = k_{abs}(1 - 10^{-\varepsilon \times l \times [S_0]}) + k_{RISC}[T_1] - (k_{ISC} + k_{nr,S_1} + k_{nr,S_1})[S_1]$
$^3PC^*$ (T_1)	$\frac{d[T_1]}{dt} = k_{ISC}[S_1] - k_{RISC}[T_1] - k_{PET,1}[T_1][HNu254] - k_{PET,2}[T_1][\text{Borate V}] - k_{PET,3}[T_1][DMAEAc] - k_{q,1}[T_1][UVA1] - k_{q,2}[T_1][UVA2]$
$^2PC^{\bullet+}$ (DC)	$\frac{d[DC]}{dt} = k_{PET,1}[T_1][HNu254] - k_{ET,1}[DC][\text{Borate V}]$
$^2PC^{\bullet-}$ (DA)	$\frac{d[DA]}{dt} = k_{PET,2}[T_1][\text{Borate V}] - k_{ET,2}[DA][\text{HNu 254}]$
HNu 254	$\frac{d[HNu254]}{dt} = -k_{PET,1}[T_1][HNu254] - k_{ET,2}[DA][\text{HNu 254}]$
Phenyl radical (PR)	$\frac{d[PR]}{dt} = k_{PET,1}[T_1][HNu254] + k_{ET,2}[DA][\text{HNu 254}]$
Borate V	$\frac{d[\text{Borate V}]}{dt} = -k_{PET,2}[T_1][\text{Borate V}] - k_{ET,1}[DC][\text{Borate V}]$
Boranyl radical (BR)	$\frac{d[BR]}{dt} = k_{PET,2}[T_1][\text{Borate V}] + k_{ET,1}[DC][\text{Borate V}] - k_{disso.}[BR]$
Alkyl radical (AR)	$\frac{d[AR]}{dt} = k_{disso.}[BR]$
DMAEAc	$\frac{d[DMAEAc]}{dt} = -k_{PET,3}[T_1][DMAEAc] - k_{amino.}[DRC][DMAEAc]$
$DMAEAc^{\bullet+}$ (DRC)	$\frac{d[DRC]}{dt} = k_{PET,3}[T_1][DMAEAc] - k_{amino.}[DRC][DMAEAc]$
DMAEAc• (DAR)	$\frac{d[DAR]}{dt} = k_{amino.}[DRC][DMAEAc]$
UVA-1 (UVA1)	$\frac{d[UVA1]}{dt} = -k_{q,1}[T_1][UVA1]$
UVA-2 (UVA2)	$\frac{d[UVA2]}{dt} = -k_{q,2}[T_1][UVA2]$
Counts of radical generation (RG)	$\frac{d[RG]}{dt} = k_{PET,1}[T_1][HNu254] + k_{ET,2}[DA][\text{HNu 254}] + k_{disso.}[BR] + k_{amino}[DRC]$

Supplementary Table 5 Rate constants for all reactions in visible-light driven PIS for the kinetic simulation. All rate constants were obtained from experimental/computational methods in the this work or were referred to literature.[3,10]

Reaction	Previous PIS (4Cz-IPN and DMAEAc)	Newly designed PIS (4DP-IPN and HNu 254 / Borate V)
Photoexcitation: k_{abs} (a.u.) PC → ^{1}PC*	7.6×10^{-3} [a]	7.6×10^{-3} [a]
Radiative decay from S_1*:* k_r (s^{-1}) ^{1}PC* → PC	2.7×10^{7} [a]	3.1×10^{7} [a]
Non-radiative decay from S_1*:* k_{nr} (s^{-1}) ^{1}PC* → PC	1.5×10^{7} [a]	8.9×10^{7} [a]
Intersystem crossing from S_1 *to* T_1*:* k_{ISC} (s^{-1}) ^{1}PC* → ^{3}PC*	1.5×10^{7} [a]	3.5×10^{8} [a]
Reverse intersystem crossing from ^{3}*PC** *to* S_1*:* k_{RISC} (s^{-1}) ^{3}PC* → ^{1}PC*	3.3×10^{5} [a]	5.5×10^{4} [a]
PET from ^{3}*PC** *to HNu 254:* $k_{PET,1}$ ($M^{-1}\cdot s^{-1}$) ^{3}PC* + HNu 254 → ^{2}PC$^{\bullet+}$ + Phenyl radical + Aryl iodide	–	2.0×10^{9}
ET from Borate V to ^{2}*PC*$^{\bullet+}$*:* $k_{ET,1}$ ($M^{-1}\cdot s^{-1}$) ^{2}PC$^{\bullet+}$ + Borate V → PC + Boranyl radical	–	2.8×10^{7}
PET from Borate V to ^{3}*PC***:* $k_{PET,2}$ ($M^{-1}\cdot s^{-1}$) ^{3}PC* + Borate V → ^{2}PC$^{\bullet-}$ + Boranyl radical	–	2.7×10^{6}
ET from ^{2}*PC*$^{\bullet-}$ *to HNu 254:* $k_{ET,2}$ ($M^{-1}\cdot s^{-1}$) ^{2}PC$^{\bullet-}$ + HNu 254 → PC + Phenyl radical + Aryl iodide	–	6.5×10^{10}
PET from DMAEAc to ^{3}*PC***:* $k_{PET,3}$ ($M^{-1}\cdot s^{-1}$) ^{3}PC* + DMAEAc → ^{2}PC$^{\bullet-}$ + DMAEAc$^{\bullet+}$	2.1×10^{7}	–
C-B bond dissociation of boranyl radical: $k_{disso.}$ (s^{-1}) Boranyl radical → Alkyl radical + Triphenyl borane	–	1.0×10^{11} [b]
^{3}*PC** *quenching by UVA-1:* $k_{q,1}$ ($M^{-1}\cdot s^{-1}$)	3.2×10^{9}	1.8×10^{8}
^{3}*PC** *quenching by UVA-2:* $k_{q,2}$ ($M^{-1}\cdot s^{-1}$)	7.5×10^{8}	2.3×10^{8}
Amino radical formation of DMAEAc$^{\bullet+}$*:* $k_{amino.}$ ($M^{-1}\cdot s^{-1}$) DMAEAc$^{\bullet+}$ + DMAEAc → DMAEAc-H$^+$ + DMAEAc •	2.3×10^{5}	–

a: Photophysical parameters of 4Cz-IPN and 4DP-IPN were from Supplementary Table 1 studied in previous work.[3]
b: Rate constants of C-B bond dissociation in boranyl radical was approximated as ~ 1.0×10^{11} s^{-1}.[10]

■ **Derivation of k_{abs}**

Our LED setups are based on 452 nm (I_0 = 10 mW/cm^2) LEDs, therefore with consideration of photonflux (m^{-2}·s^{-1}), the time-dependent concentration of S_1 excited state can be expressed by following equation (3),[11,12]

$$\frac{d[S_1]}{dt} = \phi \times \frac{A}{V_0 N_A} \times \frac{I_0}{h\nu} \times \varepsilon c l \times F, \quad \text{where F is photo kinetic factor, } F = \frac{1-10^{-\varepsilon c l}}{\varepsilon c l} \tag{3}$$

where ϕ is quantum yield of the transformation for $S_0 \rightarrow S_1$, A is cross-sectional area (100 cm^2), V_0 is the reaction volume (5 mL), N_A is Avogadro number, h is Planck constant, ν is frequency of the photon, ε is the extinction coefficient of PCs in ethyl acetate (ε_{452nm} = 7.8 × 10^3 M^{-1}·cm^{-1} for 4DP-IPN and ε_{452nm} = 2.1 × 10^3 M^{-1}·cm^{-1} for 4Cz-IPN), c is the concentration of PC (i.e., [S_0] = 4.75 × 10^{-5} M for the 10 ppm in the synthesis of poly(EHA)) and l is the optical path length (50 μm). Because it is tricky to evaluate all the factors affecting photonflux such as a vial's curvature/refractive index, they are excluded in this kinetic simulation. Quantum yield (ϕ) for $S_0 \rightarrow S_1$ is assumed as unity, hence, equation (3) can be converted to equation (4).

$$\frac{d[S_1]}{dt} = k_{abs} \times \left(1 - 10^{-0.005\ cm \times \varepsilon_{452nm} \times [S_0]}\right) = 7.6 \times 10^{-3}\ \mathrm{M \cdot s^{-1}} \times \left(1 - 10^{-0.005\ cm \times \varepsilon_{452nm} \times [S_0]}\right) \tag{4}$$

■ **Evaluation of k_{PET} and k_q**

To obtain the rate constant of PET between ^{3}PC* and co-initiators and those of ^{3}PC* quenching with UVAs, we monitored the change of delayed fluorescence of PCs along with addition of quenchers. In their Stern-Volmer plots (Supplementary Fig. 4 and 5), a linear relationship was observed.

■ **Evaluation of k_{ET}**

Because k_{ET} is the rate constants in dark reaction, it is tricky to estimate the rate constants from the direct experimental observation, therefore, we indirectly evaluated k_{ET} with computational and experimental methods (see below) using Marcus−Savéant theory where the rate constant of electron transfer can be described by following equations,[13,14]

$$k_{ET} = Z \exp\left(-\frac{\Delta G^{\ddagger}}{RT}\right) \tag{5}$$

$$\Delta G^{\ddagger} = \frac{D_{R-X} + \lambda}{4}\left(1 + \frac{\Delta G^{\circ}}{D_{R-X} + \lambda}\right)^2 \tag{6}$$

$$\Delta G^{\ddagger} \approx \frac{D_{R-X}}{4}\left(1 + \frac{\Delta G^{\circ}}{D_{R-X}}\right)^2 \quad \text{for concerted electron transfer} \tag{7}$$

$$\Delta G^{\ddagger} \approx \frac{\lambda}{4}\left(1 + \frac{\Delta G^{\circ}}{\lambda}\right)^2 \quad \text{for stepwise electron transfer} \tag{8}$$

where Z is the pre-exponential factor, $\Delta G^{\ddagger}$ is the activation energy of the reaction, ΔG° is the driving force of the reaction, D_{R-X} is the bond dissociation energy and λ is the external (solvent) reorganization energy.

a ■ Summary of the experimental and calculated values in concerted electron transfer process

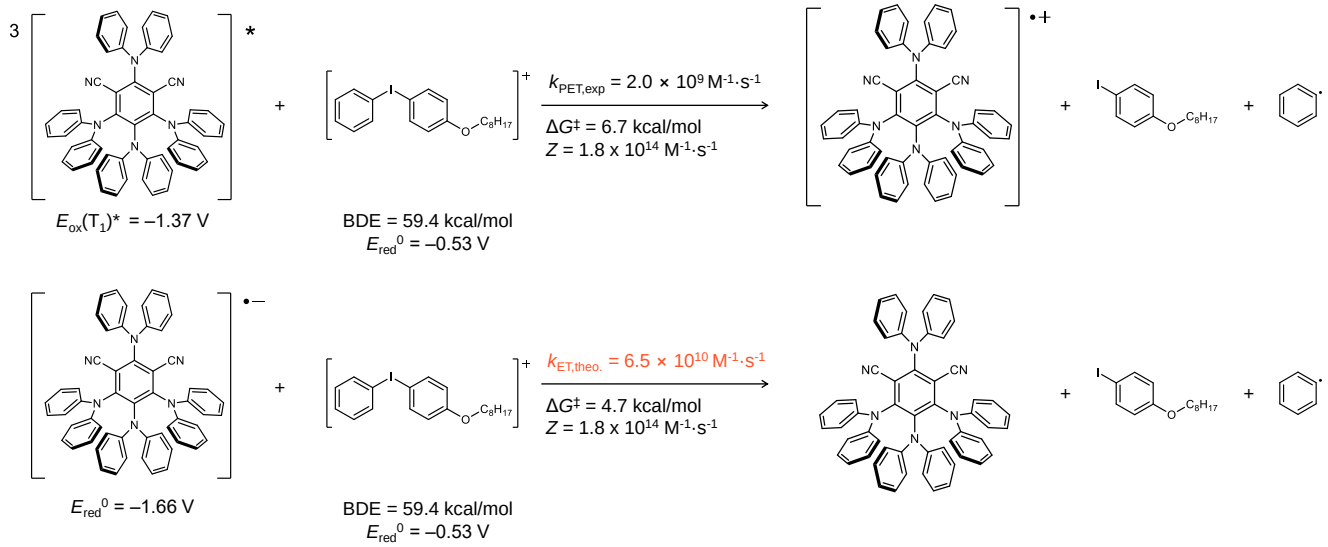

b ■ Summary of the experimental and calculated values in stepwise electron transfer process

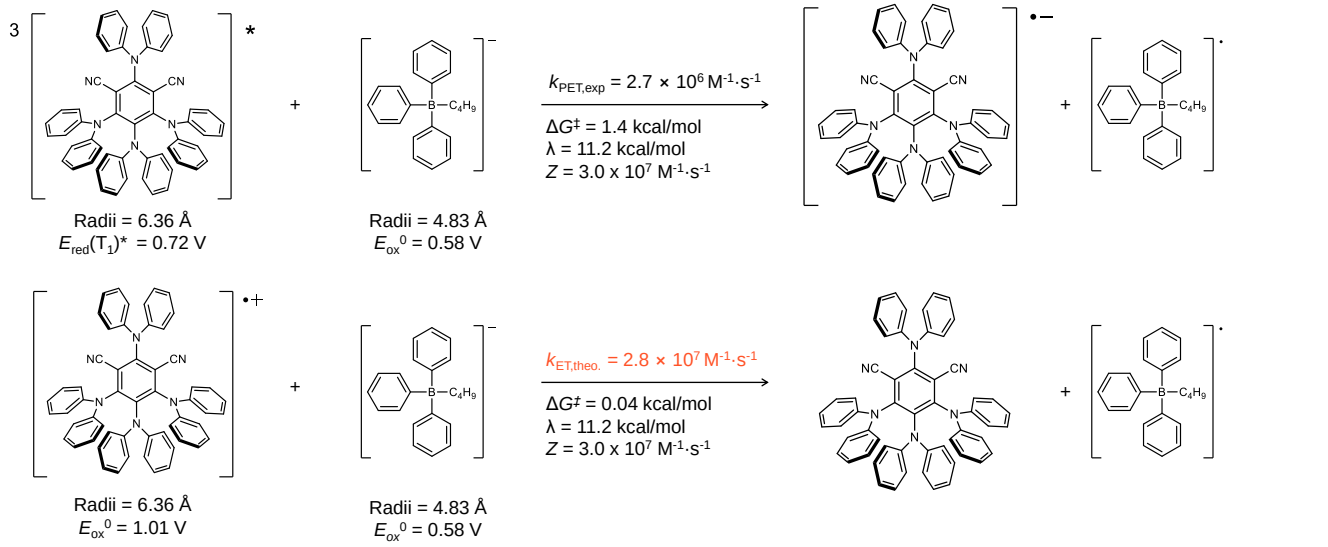

Supplementary Fig. 8 Summary of the experimental and calculated values to obtain the rate constant for electron transfer between 4DP-IPN and co-initiators; molecular radii of each species are calculated by DFT calculations using the Gaussian16 program package, Z is the pre-exponential factor, $\Delta G^{\ddagger}$ is the activation energy of the electron transfer reaction, and λ is the external (solvent) reorganization energy.

■ Evaluation of reorganization energy

For the concerted electron transfer process, the reorganization energy, λ, can be approximated to bond dissociation energy (D_{R-X}).[14] Therefore, to obtain the rate constant of electron transfer between $PC^{\bullet-}$ and iodonium cation, the bond dissociation energy of iodonium was referred as D_{R-X} = 59.4 kcal/mol.[15] Meanwhile, for the stepwise electron transfer between $PC^{\bullet+}$ and borate anion, because there is no significant change of molecular size of involved chemicals, internal reorganization energy, λ_i, is fairly negligible. Hence, the sum of reorganization energy, λ, was approximated to only external (solvent) reorganization energy, $\lambda = \lambda_i + \lambda_o \approx \lambda_o$.[13]

$$\lambda_o = \frac{e^2}{4\pi\varepsilon_0}\left(\frac{1}{\varepsilon_{op}} - \frac{1}{\varepsilon_s}\right)\left(\frac{1}{2r_A} + \frac{1}{2r_B} - \frac{1}{r_A + r_B}\right) \quad (9)$$

where e is the electron charge, ε_0 is the vacuum permittivity, ε_{op} and ε_s are the solvent optical and static dielectric constants, respectively. The r_s are the radii of the equivalent spheres of the subscript species. We calculated the radii of each species (Supplementary Fig. 8) with DFT calculations.

■ Evaluation of pre-exponential factor, *Z*

Because the size difference among PC species (i.e., $^3PC^*$, $PC^{\bullet-}$ and $PC^{\bullet+}$) is negligible, the pre-exponential factor, *Z*, for electron transfer between PC species and co-initiators can be obtained from the rate constant for PET between $^3PC^*$ to co-initiators within reductive and oxidative quenching cycle, respectively (Supplementary Fig. 8).[2]

The equations (5–8) can provide the pre-exponential factor for PET between $^3PC^*$ and co-initiators using the reorganization energy, λ, and the driving force, ΔG. These pre-exponential factor values should be same for the electron transfer between $^3PC^*$ and co-initiators in the same manner. It is notable that the previously reported pre-exponential factor, *Z*, is ~10^{11} $M^{-1}s^{-1}$,[16,17] thus, our k_{ET} might be under/overestimated and this discrepancy might be from the inaccurate extraction of values from experimental results. Nevertheless, our kinetic simulations were appropriately modeled to analyze the relative population of each species.

■ Evaluation of $k_{amino.}$

The α-amino radical species are generated from the oxidized tertiary amines associated with intramolecular proton transfer to neutral tertiary amines.[18] Hence, we evaluated the bimolecular rate constant from the activation energy ($\Delta G^{\ddagger}_{calc}$) for α-amino radical generation at RT using following Eyring equation (10) (Supplementary Fig. 9).[3]

$$k = \kappa\frac{k_B T}{h}\, e^{-\frac{\Delta G^{\ddagger}}{RT}} \quad (10)$$

where k_B is the Boltzmann constant, T is the temperature, h is the Planck constant, and κ is the transmission coefficient and is assumed as a unity. In the case of DMAEAc, the activation energy is calculated as $\Delta G^{\ddagger}_{calc.}$ = 10.15 kcal/mol and the rate constant of α-amino radical generation is evaluated as $k_{amino.}$ = 2.3 × 10^5 $M^{-1}\cdot s^{-1}$.

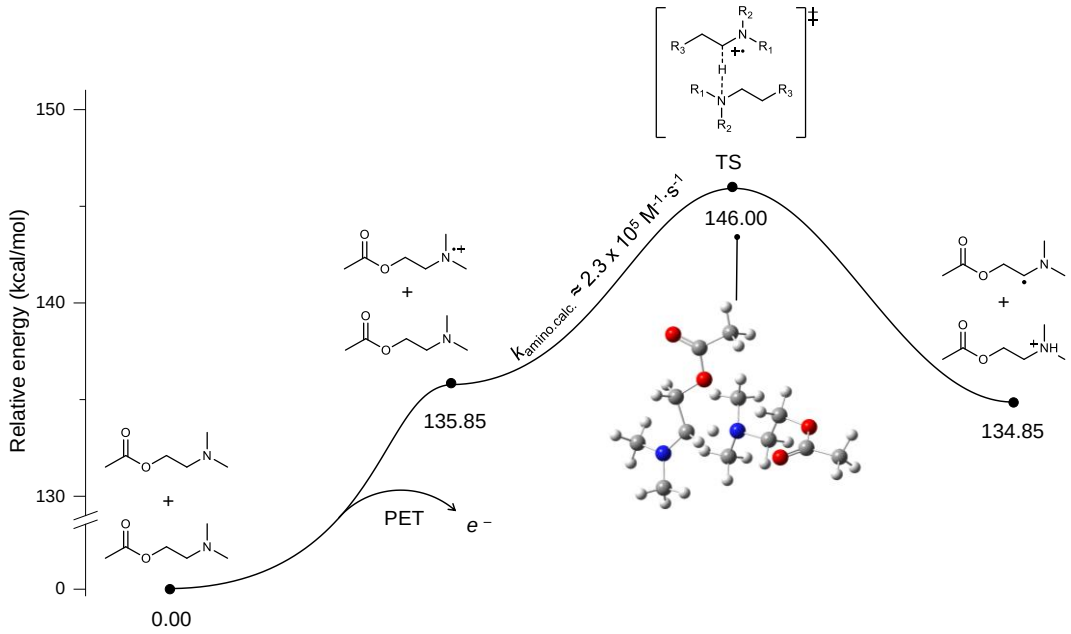

Supplementary Fig. 9 Energy profiles for α-amino radical generation from DMAEAc$^{\bullet+}$ using DFT calculation. The rate constant for α-amino radical generation was evaluated with Eyring equation at RT.

Supplementary Note 3. Visible-light driven PIS for synthesis of UV-blocking OCAs

3.1. Characterization of adhesive film

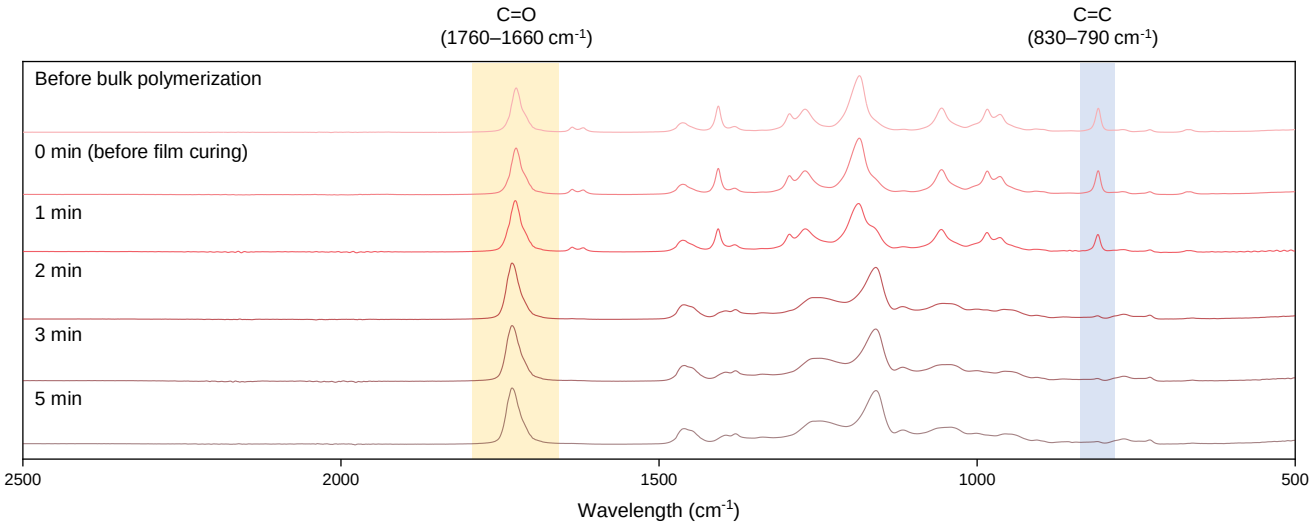

FR-IR spectra of a representative OCA preparation. The prepared OCA was conducted with [EHA]:[HBA] = 3:1 using 4DP-IPN (3 ppm), HNu 254 (1000 ppm) and Borate V (600 ppm).

Conversion of monomers from FT-IR spectra was calculated by following equation (11),

$$\text{Conversion (\%)} = \frac{\frac{A_{0(C=C)}}{A_{0(C=O)}} - \frac{A_{t(C=C)}}{A_{t(C=O)}}}{\frac{A_{0(C=C)}}{A_{0(C=O)}}} \times 100 \qquad (11)$$

where $A_{0(C=C)}$, $A_{0(C=O)}$, $A_{t(C=C)}$ and $A_{t(C=O)}$, denote integrated area of representative peaks of C=C (830-790 cm^{-1}) at initial time, C =O (1760-1660 cm^{-1}) at initial time, C=C at time *t*, and C=O time at time *t*, respectively. If the integrated area is negative, the monomer conversion was approximated as 100%.

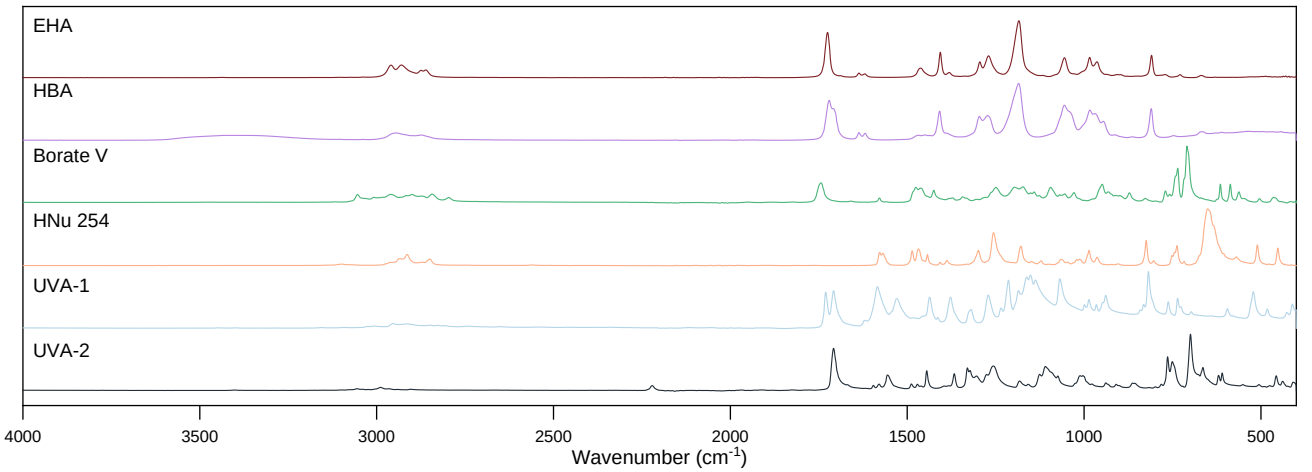

FT-IR spectra data of monomers, co-initiators and UVAs.

3.2. Synthesis of UV-blocking OCAs

Supplementary Table 6 Results of previous PIS (with [BA]:[HBA] = 4:1) for UV-blocking OCAs using 4Cz-IPN and tertiary amines. PIS reaction conditions were followed the general procedures to prepare acrylic syrup and film curing. All conversions were determined by FT-IR.

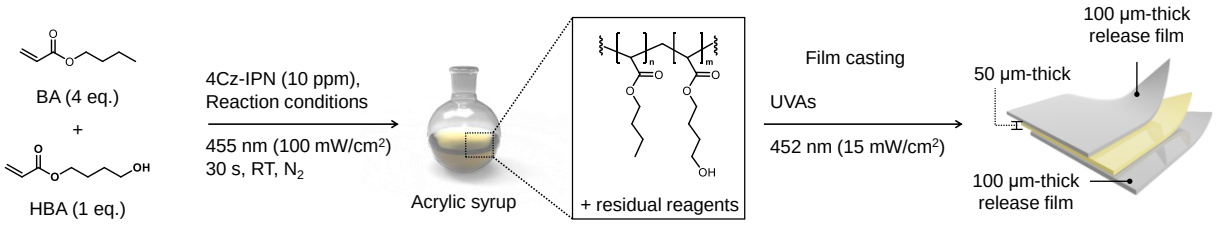

Entry	Co-initiator (ppm)	UVA (ppm)		Time $_{Film}$ (min)	Dosage $_{Film}$ (mJ/cm^2)	Conversion $_{FT-IR}$ (%)	
		UVA-1	UVA-2			Acrylic syrup	Film
1	DMAEAc (5000)	–	–	4	3600	10.7[a]	95.1
2	DMAEAc (5000)	1500 (0.3 phr)	–	10	9000	10.7[a]	97.7
3	DMAEAc (5000)	–	4800 (1 phr)	20	18000	10.7[a]	96.3
4	DMAEAc (5000)	1500 (0.3 phr)	4800 (1 phr)	30	27000	10.7[a]	95.7
5	DMAEAc (5000)	–	–	5	3000[b]	11.4	94.4[b]
6	DMAEAc (5000)	1500 (0.3 phr)	–	20	12000[b]	11.4	94.1[b]
7	DMAEAc (5000)	–	4800 (1 phr)	20	12000[b]	11.4	95.3[b]
8	DMAEAc (5000)	1500 (0.3 phr)	4800 (1 phr)	30	18000[b]	11.4	94.7[b]
9	DMAEAc (2000) DMAEA (3000)	–	–	6	5400	11.9	95.9
10	DMAEAc (2000) DMAEA (3000)	1500 (0.3 phr)	4800 (1 phr)	30	27000	11.9	96.1

a: bulk polymerization was conducted under air in closed vial.
b: film curing was conducted under 452 nm (10 mW/cm^2).

Supplementary Table 7 Results of newly designed PIS (with [EHA]:[HBA] = 3:1) using 4Cz-IPN, HNu 254 and Borate V. PIS reaction conditions were followed the general procedures to prepare acrylic syrup and film curing. All conversions were determined by FT-IR.

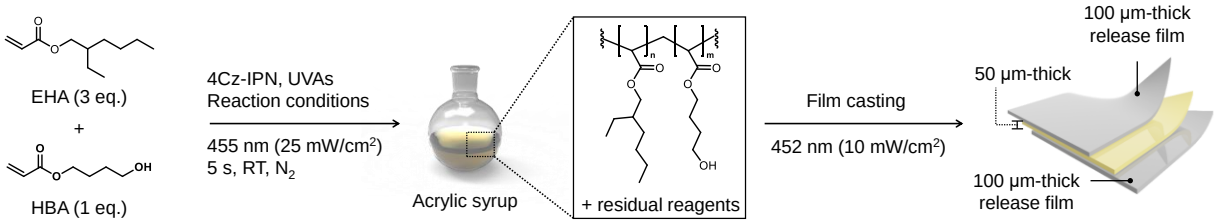

Entry	PC	PC loading (ppm)	Co-initiator (ppm)		UVA (ppm)		Dosage Film (mJ/cm²)	Conversion FT-IR (%)	
			HNu 254	Borate V	UVA-1	UVA-2		Acrylic syrup	Film
1	4Cz-IPN	1	500	300	–	–	6000	2.4	96.6
2	4Cz-IPN	1	500	300	2000 (0.3 phr)	–	12000	1.0	98.0
3	4Cz-IPN	1	500	300	–	6400 (1 phr)	12000	1.2	100
4	4Cz-IPN	1	500	300	2000 (0.3 phr)	6400 (1 phr)	18000	2.2[a]	100
5	4Cz-IPN	10	500	300	–	–	3000	10.3	94.3
6	4Cz-IPN	10	500	300	2000 (0.3 phr)	–	4800	2.1	96.9
7	4Cz-IPN	10	500	300	–	6400 (1 phr)	4800	5.1	93.4
8	4Cz-IPN	10	500	300	2000 (0.3 phr)	6400 (1 phr)	6000	4.6[a]	97.7
9	4Cz-IPN	10	1000	600	–	–	1800	10.9	98.9
10	4Cz-IPN	10	1000	600	2000 (0.3 phr)	–	3000	3.3	98.6
11	4Cz-IPN	10	1000	600	–	6400 (1 phr)	3000	5.2	97.3
12	4Cz-IPN	10	1000	600	2000 (0.3 phr)	6400 (1 phr)	3600	7.6[a]	99.3

a: bulk polymerization was conducted for 10 s due to slow polymerization.

Supplementary Table 8 Results of newly designed PIS (with [EHA]:[HBA] = 3:1) using 4DP-IPN (1–3 ppm), HNu 254 (500–1000 ppm) and Borate V (300–600 ppm). PIS reaction conditions were followed the general procedures to prepare acrylic syrup and film curing. All conversions were determined by FT-IR.

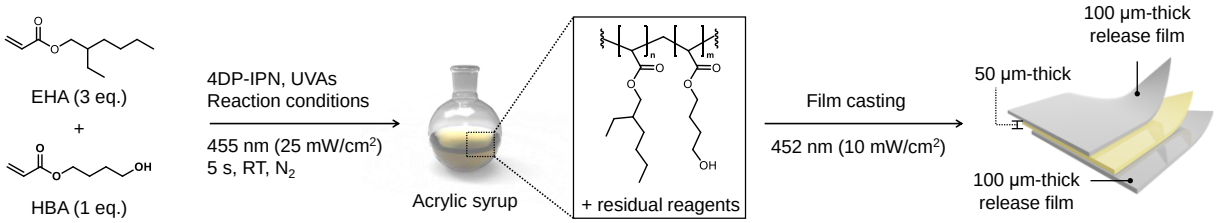

Entry	PC	PC loading (ppm)	Co-initiator (ppm)		UVA (ppm)		Dosage Film (mJ/cm²)	Conversion FT-IR (%)	
			HNu 254	Borate V	UVA-1	UVA-2		Acrylic syrup	Film
1	4DP-IPN	1	500	300	–	–	3000	9.6	97.5
2	4DP-IPN	1	500	300	2000 (0.3 phr)	–	6000	3.5	99.5
3	4DP-IPN	1	500	300	–	6400 (1 phr)	9000	2.3	96.2
4	4DP-IPN	1	500	300	2000 (0.3 phr)	6400 (1 phr)	6000	6.0[a]	97.4
5	4DP-IPN	2	1000	600	–	–	1800	19.3	98.5
6	4DP-IPN	2	1000	600	2000 (0.3 phr)	–	1800	15.9	94.9
7	4DP-IPN	2	1000	600	–	6400 (1 phr)	3000	16.7	94.9
8	4DP-IPN	2	1000	600	2000 (0.3 phr)	6400 (1 phr)	3000	10.8	98.0
9	4DP-IPN	3	1000	600	–	–	600	13.5[b]	97.8
10	4DP-IPN	3	1000	600	2000 (0.3 phr)	–	1800	9.5	100
11	4DP-IPN	3	1000	600	–	6400 (1 phr)	3000	8.9	100
12	4DP-IPN	3	1000	600	2000 (0.3 phr)	6400 (1 phr)	2400	8.3	97.8

a: bulk polymerization was conducted for 10 s due to slow polymerization.
b: bulk polymerization was conducted for 2 s due to fast polymerization.

Supplementary Table 9 Results of control experiments with newly designed PIS (with [EHA]:[HBA] = 3:1) using PC (4DP-IPN (3 ppm) or 4Cz-IPN (10 ppm)), HNu 254 (1000 ppm) and Borate V (600 ppm). PIS reaction conditions were followed the general procedures to prepare acrylic syrup and film curing. All conversions were determined by FT-IR.

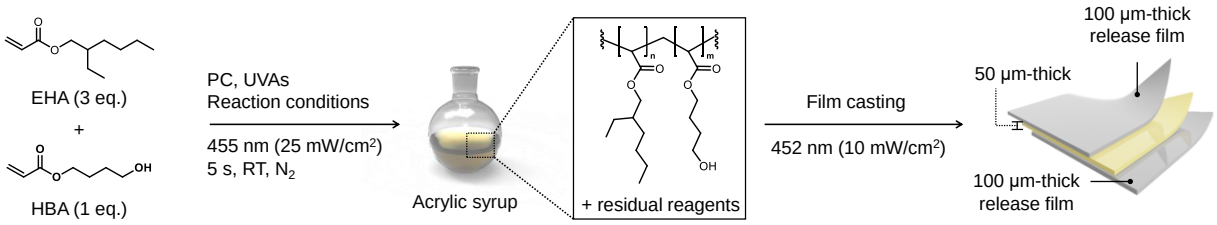

Entry	PC	PC loading (ppm)	Co-initiator (ppm)		UVA (ppm)		Dosage $_{Film}$ (mJ/cm^2)	Conversion $_{FT-IR}$ (%)	
			HNu 254	Borate V	UVA-1	UVA-2		Acrylic syrup	Film
1	4DP-IPN	3	1000	–	–	–	2400	2.2	41.8
2	4DP-IPN	3	1000	–	2000 (0.3 phr)	–	2400	2.4	65.1
3	4DP-IPN	3	1000	–	–	6400 (1 phr)	2400	2.4	3.0
4	4DP-IPN	3	1000	–	2000 (0.3 phr)	6400 (1 phr)	2400	0.3	55.1
5	4DP-IPN	3	–	600	–	–	2400	0.3	0.8
6	4DP-IPN	3	–	600	2000 (0.3 phr)	–	2400	0.3	1.9
7	4DP-IPN	3	–	600	–	6400 (1 phr)	2400	0.2	1.5
8	4DP-IPN	3	–	600	2000 (0.3 phr)	6400 (1 phr)	2400	0.3	0.6
9	4Cz-IPN	10	1000	–	–	–	2400	1.9	80.7
10	4Cz-IPN	10	1000	–	2000 (0.3 phr)	–	2400	0.3	25.6
11	4Cz-IPN	10	1000	–	–	6400 (1 phr)	2400	1.0	19.7
12	4Cz-IPN	10	1000	–	2000 (0.3 phr)	6400 (1 phr)	2400	0.8	20.6
13	4Cz-IPN	10	–	600	–	–	2400	0.9	61.9
14	4Cz-IPN	10	–	600	2000 (0.3 phr)	–	2400	0.2	22.5
15	4Cz-IPN	10	–	600	–	6400 (1 phr)	2400	0.7	7.6
16	4Cz-IPN	10	–	600	2000 (0.3 phr)	6400 (1 phr)	2400	0.3	14.1

Supplementary Table 10 Reproducibility test of previous PIS (with [BA]:[HBA] = 4:1) using 4Cz-IPN (10 ppm) and tertiary amines (5000 ppm). PIS reaction conditions were followed the general procedures to prepare acrylic syrup and film curing. All conversions were determined by FT-IR.

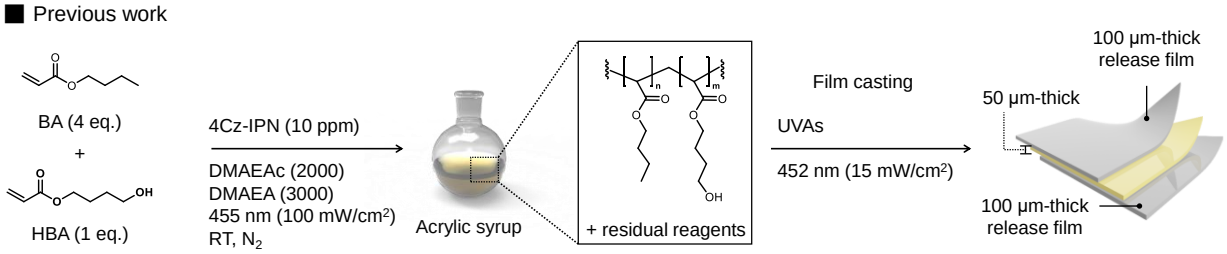

Entry	UVA (ppm)	Dosage $_{\text{Acrylic syrup}}$ (mJ/cm^2)	Conversion $_{\text{Acrylic syrup}}$ (%)	Dosage $_{\text{Film}}$ (mJ/cm^2)	Conversion $_{\text{Film}}$ (%)
1			15.3		95.3
2			15.0		95.3
3	-	3000	15.0	5400	95.8
4			15.3		94.7
5			15.0		95.4
6			15.3		96.1
7	UVA-1 (1500)		15.0		95.4
8	UVA-2 (4800)	3000	15.0	27000	94.6
9			15.3		97.3
10			15.0		91.2

Supplementary Table 11 Reproducibility test of newly designed PIS (with [EHA]:[HBA] = 3:1) using 4DP-IPN (3 ppm), HNu 254 (1000 ppm) and Borate V (600 ppm). PIS reaction conditions were followed the general procedures to prepare acrylic syrup and film curing. All conversions were determined by FT-IR.

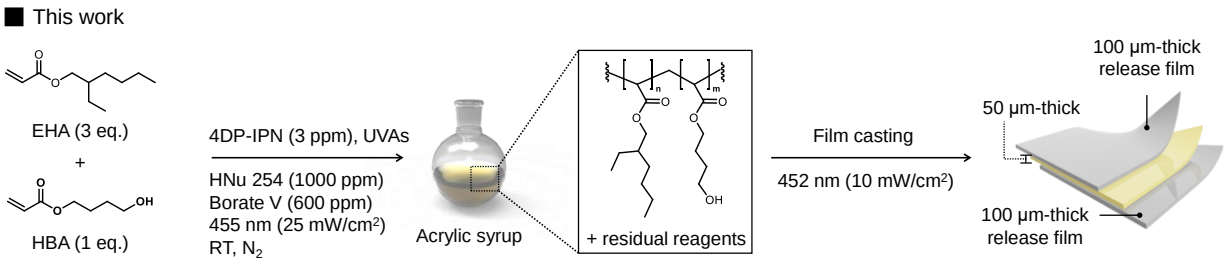

Entry	UVA (ppm)	Dosage $_{\text{Acrylic syrup}}$ (mJ/cm^2)	Conversion $_{\text{Acrylic syrup}}$ (%)	Dosage $_{\text{Film}}$ (mJ/cm^2)	Conversion $_{\text{Film}}$ (%)
1			13.6		98.4
2			13.7		96.3
3	-	50	12.9	600	96.8
4			13.1		97.5
5			14.2		99.8
6			8.3		97.8
7	UVA-1 (1500)		7.3		94.6
8	UVA-2 (4800)	125	7.7	2400	100
9			8.1		98.4
10			7.6		99.9

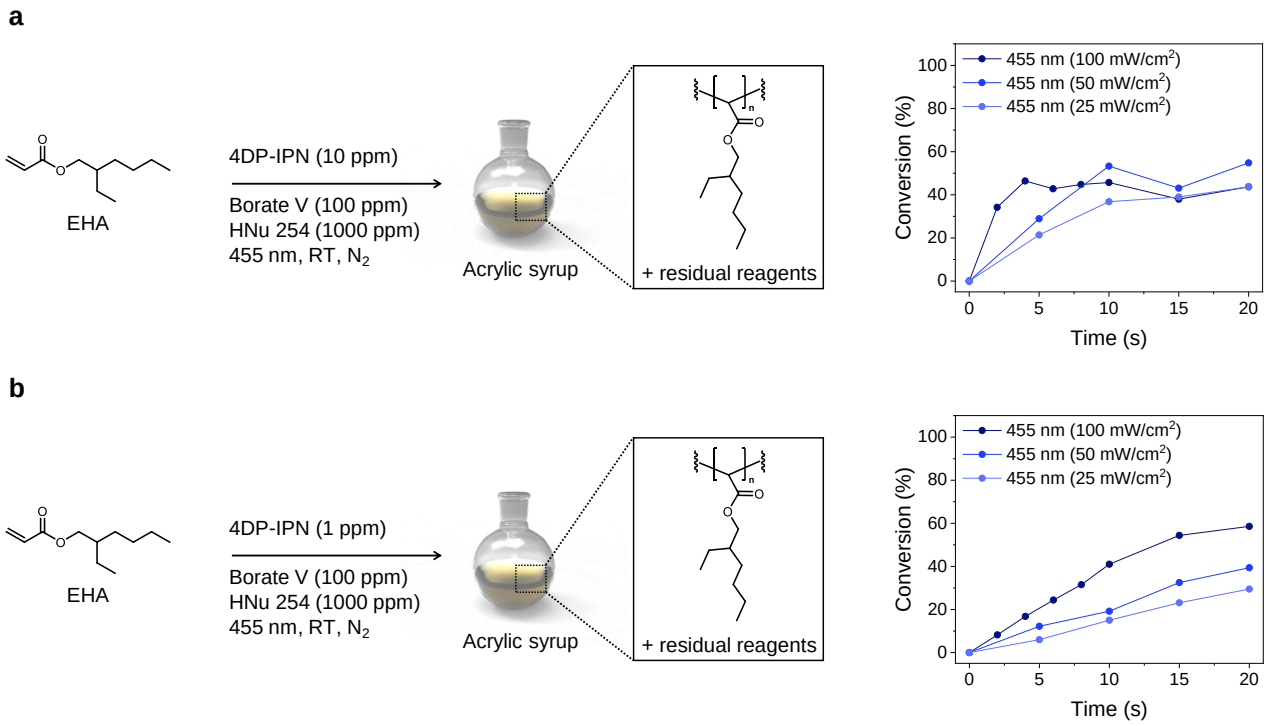

Supplementary Fig. 10 Conversion of acrylic syrup using 4DP-IPN, HNu254 (1000 ppm) and Borate V (100 ppm) with light intensity 455 nm (25–100 mW/cm^2). The polymerization of EHA was conducted with **a** 10 ppm (relative to monomer) and **b** 1 ppm of 4DP-IPN. All conversions were determined by FT-IR.

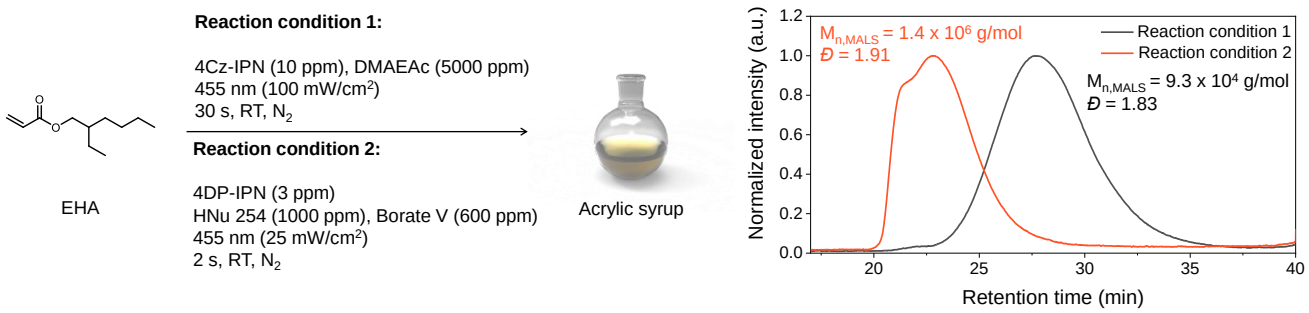

Supplementary Fig. 11 GPC trace of acrylic syrup of synthesized poly(EHA) by previous PIS (Reaction condition 1, black line) and newly designed PIS (Reaction condition 2, orange line) conditions. Molecular weight of acrylic syrup are determined by MALS detector (dn/dc = 0.0702 for poly(EHA)).[19]

Supplementary Note 4. Characterization of UV-blocking OCAs

4.1. Optical properties of UV-blocking OCAs

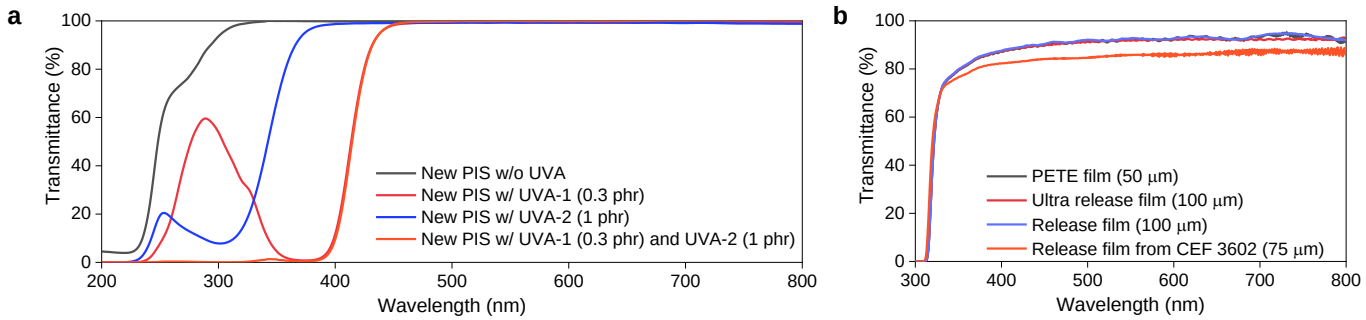

Supplementary Fig. 12 UV/vis transmission of **a** prepared OCAs synthesized following the general procedures and **b** films used in this work; PETE (50 μm, youngwoo trading), release film (silicon-treated PETE film, 100 μm, youngwoo trading), super release film (silicon-treated PETE film, 100 μm, youngwoo trading) and release film from CEF 3602 provided together to protect the OCA.

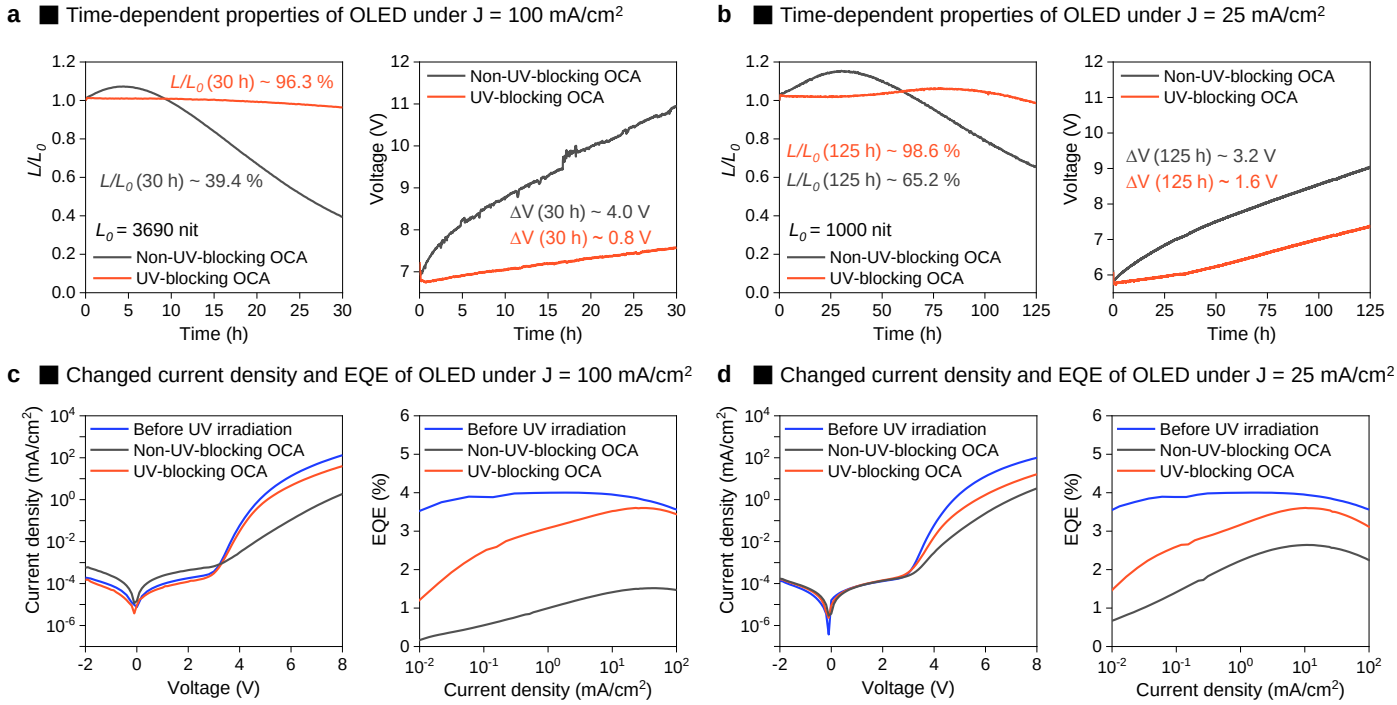

Supplementary Fig. 13 a-b Time-dependent changes of luminance (left) and voltage (right) of blue OLED covered by the prepared non-UV-blocking OCA film (black line) and UV-blocking OCA film (orange line) exposed by UV-irradiation **a** under constant current (100 mA/cm^2) and **b** under constant current (25 mA/cm^2). **c-d** Change in current density (left) and external quantum efficiency (EQE) (right) of blue OLED covered by the prepared non-UV-blocking OCA film (black line) and UV-blocking OCA film (orange line) exposed by UV irradiation over voltage **c** under constant current (100 mA/cm^2) and **d** under constant current (25 mA/cm^2). As control experiment, non-UV-irradiated OLEDs were also monitored (blue line). All measurements in electronic properties of blue OLED were recorded every 10 min.

4.2. Mechanical properties of UV-blocking OCAs

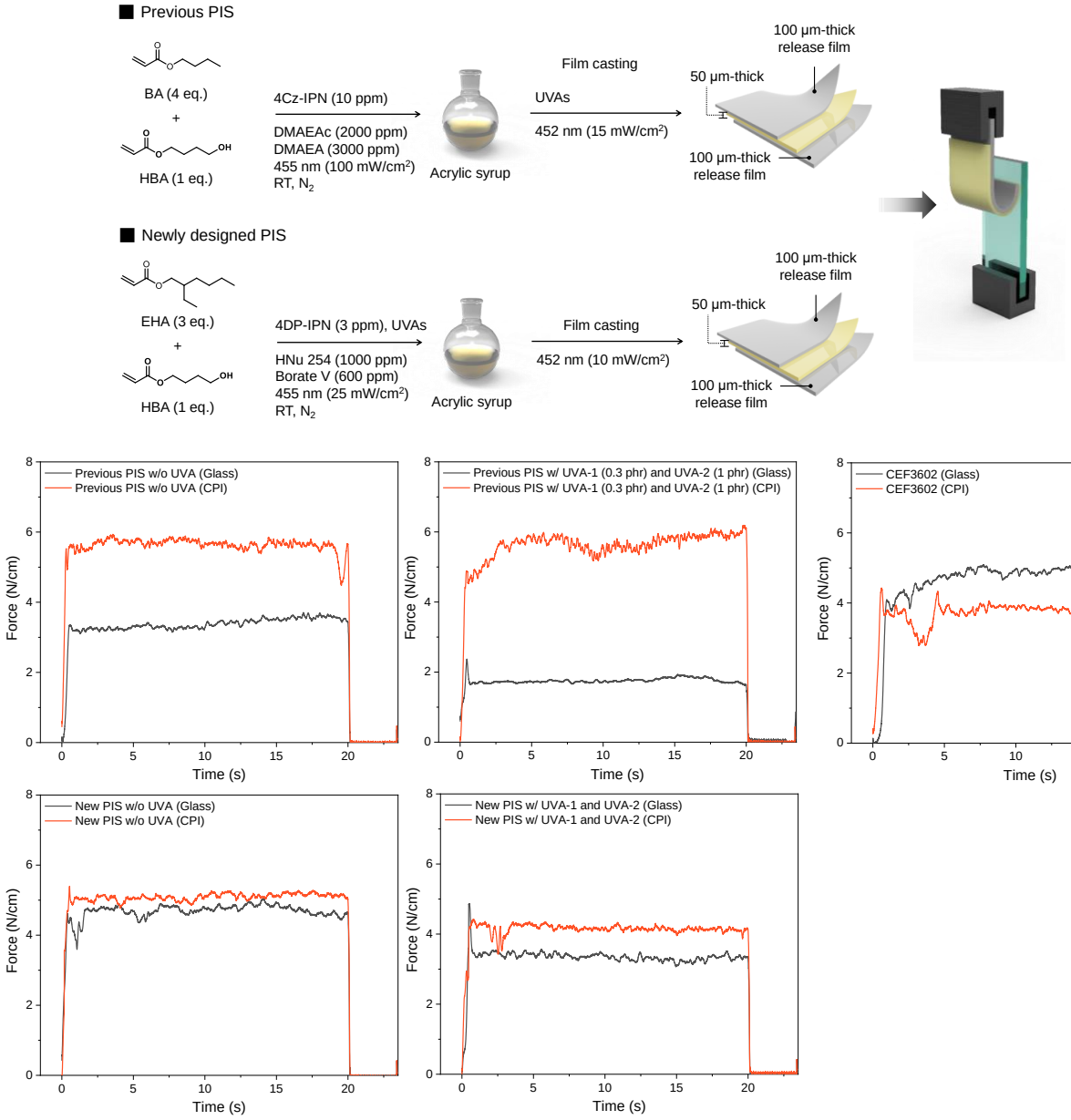

Supplementary Fig. 14 Results of peel strength of prepared OCA films by previous PIS and new PIS conditions. PIS reaction conditions were followed the general procedures to prepare acrylic syrup and film curing. The previous PIS (with [BA]:[HBA] = 4:1) were conducted with 4Cz-IPN (10 ppm), DMAEAc (2000 ppm), DMAEA (3000 ppm), UVA-1 (1500 ppm) and UVA-2 (4800 ppm). For newly designed PIS (with [EHA]:[HBA] = 3:1), 4DP-IPN (3 ppm), HNu 254 (1000 ppm), Borate V (600 ppm), UVA-1 (2000 ppm) and UVA-2 (6400 ppm) were used. Peel strengths of prepared OCA films were evaluated as the average of the measured forces in the time range (5–15 s, 5 mm/s). CEF3602 was measured as a control experiment.

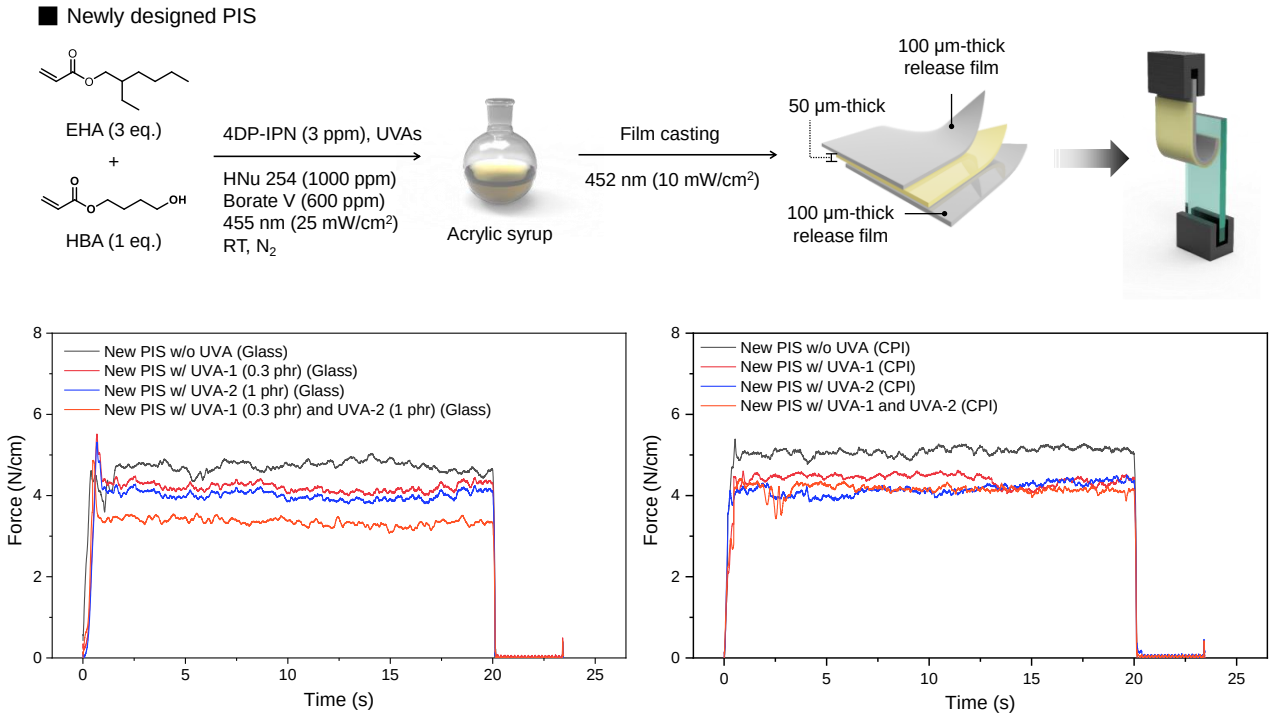

Supplementary Fig. 15 Results of peel strength of prepared OCA films by newly designed PIS with different substrates (glass or CPI). For newly designed PIS (with [EHA]:[HBA] = 3:1), 4DP-IPN (3 ppm), HNu 254 (1000 ppm), Borate V (600 ppm), UVA-1 (2000 ppm) and UVA-2 (6400 ppm) were used. Peel strengths of prepared OCA films were evaluated as the average of the measured forces in the time range (5–15 s, 5 mm/s).

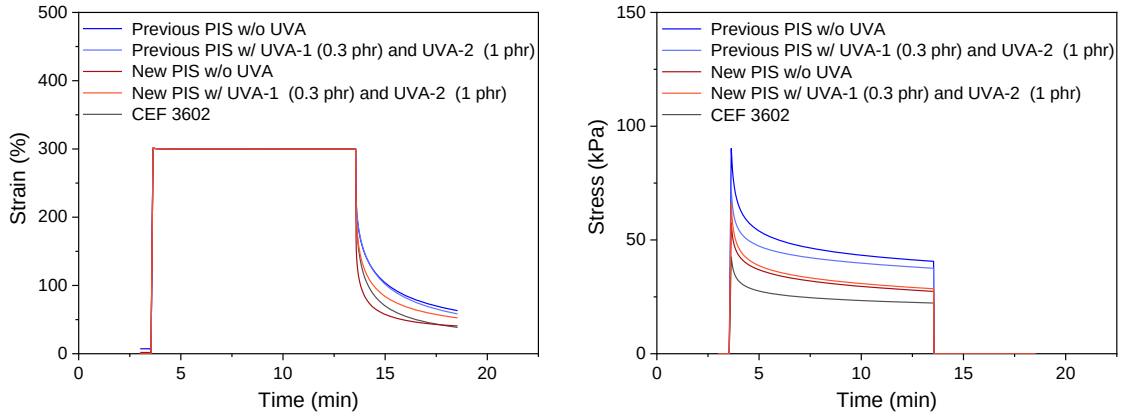

Supplementary Fig. 16 Results of stain recovery and stress relaxation of prepared OCA films by previous PIS and newly designed PIS conditions. The previous PIS (with [BA]:[HBA] = 4:1) were conducted with 4Cz-IPN (10 ppm), DMAEAc (2000 ppm), DMAEA (3000 ppm), UVA-1 (1500 ppm) and UVA-2 (4800 ppm). For newly designed PIS (with [EHA]:[HBA] = 3:1), 4DP-IPN (3 ppm), HNu 254 (1000 ppm), Borate V (600 ppm), UVA-1 (2000 ppm) and UVA-2 (6400 ppm) were used. Strain recovery and stress relaxation of prepared OCAs were evaluated at 25 ℃. After pulling the specimens with 300% strain for 10 min, they were recovered for 5 min. CEF3602 was measured as a control experiment.

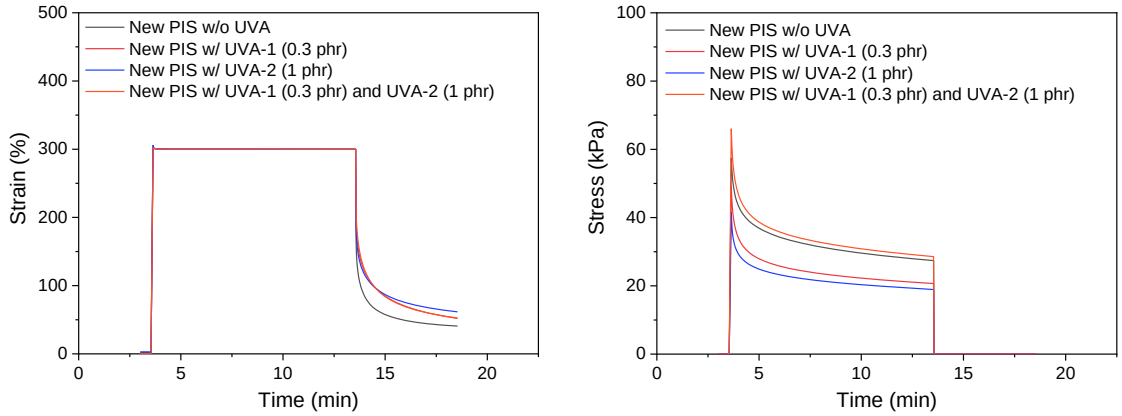

Supplementary Fig. 17 Results of strain recovery and stress relaxation of prepared OCA films by newly designed PIS along with additions of UVAs. For newly designed PIS (with [EHA]:[HBA] = 3:1), 4DP-IPN (3 ppm), HNu 254 (1000 ppm), Borate V (600 ppm), UVA-1 (2000 ppm) and UVA-2 (6400 ppm) were used. Strain recovery and stress relaxation of prepared OCAs were evaluated at 25 ℃. After pulling the specimens with 300% strain for 10 min, they were recovered for 5 min.

Supplementary Table 12 Results of storage modulus (*G*'), loss modulus (*G*''), and damping factor (tan δ) of prepared OCA films by previous PIS and newly designed PIS conditions. The previous PIS (with [BA]:[HBA] = 4:1) were conducted with 4Cz-IPN (10 ppm), DMAEAc (2000 ppm), DMAEA (3000 ppm), UVA-1 (1500 ppm) and UVA-2 (4800 ppm). For newly designed PIS (with [EHA]:[HBA] = 3:1), 4DP-IPN (3 ppm), HNu 254 (1000 ppm), Borate V (600 ppm), UVA-1 (2000 ppm) and UVA-2 (6400 ppm) were used. The viscoelastic properties of prepared OCAs were evaluated at -20 ℃, 25 ℃, 60 ℃, and 85 ℃, respectively. CEF3602 was measured as a control experiment.

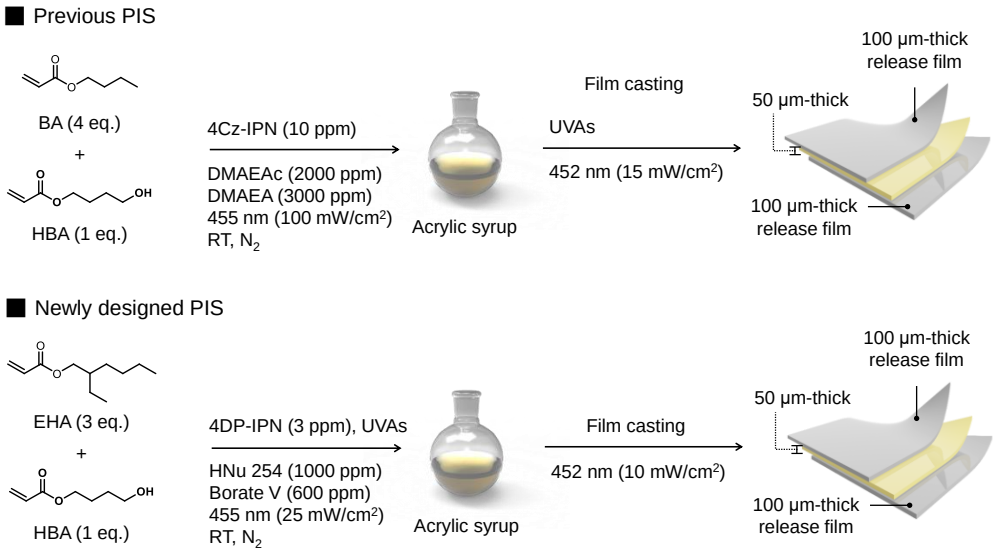

Entry	OCA	Storage modulus (*G*') (kPa)				Loss modulus (*G*'') (kPa)				Damping factor (tan δ)			
		–20 ℃	25 ℃	60 ℃	85 ℃	–20 ℃	25 ℃	60 ℃	85 ℃	–20 ℃	25 ℃	60 ℃	85 ℃
1	CEF 3602	115.0	45.3	32.3	27.6	78.8	12.4	10.0	8.7	0.69	0.27	0.31	0.32
2	Previous PIS w/o UVA	194.0	76.1	54.9	45.5	147.0	17.4	15.9	14.0	0.76	0.23	0.29	0.31
3	Previous PIS w/ UVAs	115.2	68.6	57.7	53.4	59.3	13.2	13.2	12.7	0.51	0.19	0.23	0.24
4	New PIS w/o UVA	145.0	41.2	28.0	22.8	134.6	13.4	11.1	10.0	0.93	0.33	0.40	0.44
5	New PIS w/ UVAs	150.3	45.0	36.1	32.7	145.4	11.1	8.8	8.1	0.97	0.25	0.24	0.25

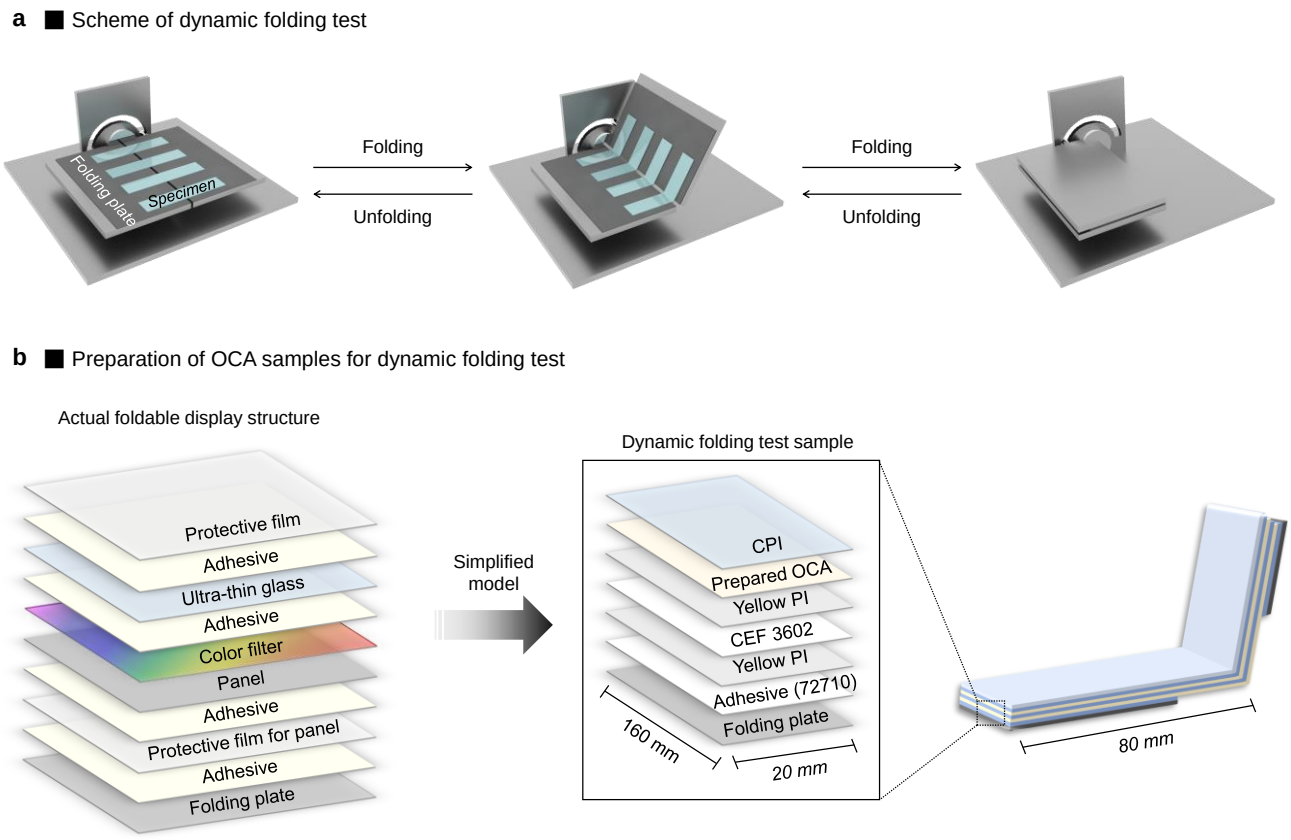

Supplementary Fig. 18 a Scheme of dynamic folding test. **b** Preparation of OCA samples for dynamic folding test. The OCA samples were prepared by stacking colorless polyimide (CPI, PI Advanced Materials, 50 μm), prepared OCA (50 μm), yellow PI (GL140A, 35 μm), CEF 3602 (3M, 50 μm), and yellow PI (GL140A, 35 μm) in this order. After preparing the sample, commercial acrylic adhesive (3M, 72710) was used as an adhesive layer to attach to the folding plate.

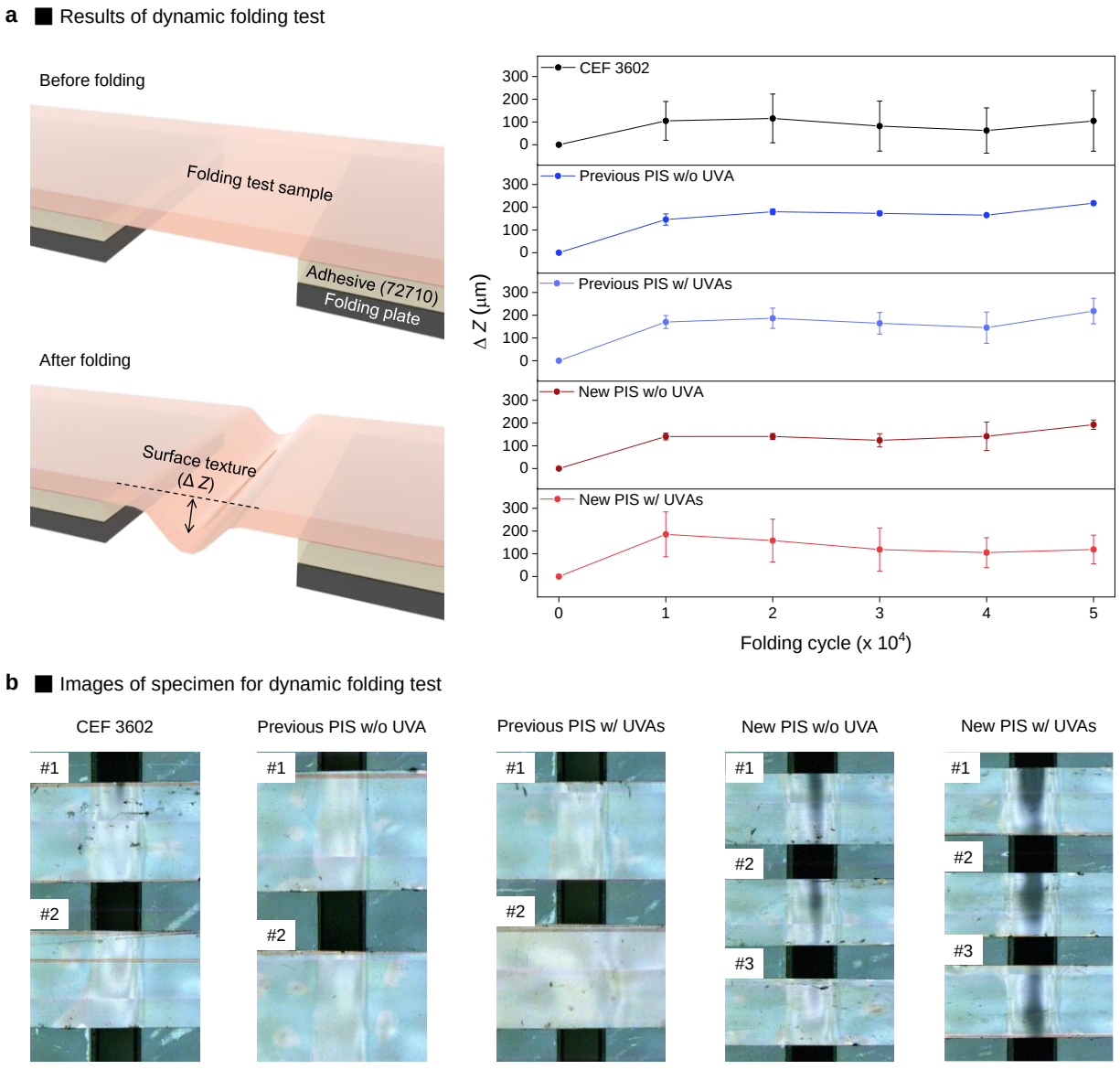

Supplementary Fig. 19 a Results of dynamic folding test. The surface texture (ΔZ) of OCA samples were measured along with folds by 5 x 10^4 times at -20 °C. CEF 3602 and previous PIS OCAs were tested with two identical samples, and new PIS OCAs were measured three identical samples. The OCA samples were cured by following conditions: the previous PIS (with [BA]:[HBA] = 4:1) were conducted with 4Cz-IPN (10 ppm), DMAEAc (2000 ppm), DMAEA (3000 ppm), UVA-1 (1500 ppm) and UVA-2 (4800 ppm) and the newly designed PIS (with [EHA]:[HBA] = 3:1) were conducted with 4DP-IPN (3 ppm), HNu 254 (1000 ppm), Borate V (600 ppm), UVA-1 (2000 ppm) and UVA-2 (6400 ppm) were used. **b** Images of specimen for dynamic folding test. No defect or delamination in the tested OCA samples were observed at -20 °C.

Supplementary References

1. Singh, V. K. *et al.* Highly efficient organic photocatalysts discovered via a computer-aided-design strategy for visible-light-driven atom transfer radical polymerization. *Nat. Catal.* **1**, 794–804 **(**2018**).**
2. Kwon, Y. *et al.* Formation and degradation of strongly reducing cyanoarene-based radical anions towards efficient radical anion-mediated photoredox catalysis. *Nat. Commun.* **14**, 1–15 (2023).
3. Back, J. *et al.* Visible light curable acrylic resins toward UV-light blocking adhesives for foldable displays. *Adv. Mater.* 2204776 (2022).
4. Roth, H. G., Romero, N. A. & Nicewicz, D. A. Experimental and calculated electrochemical potentials of common organic molecules for applications to single-electron redox chemistry. *Synlett* **27**, 714–723 (**2016**).
5. Yang, H. *et al.* Multi-layer in-situ for evaluation of dynamic mechanical properties of pressure sensitive adhesives. *Int. J. Adhes. Adhes.* **27**, 536–546 (2007).
6. Furukawa, T., Nakanotani, H., Inoue, M. & Adachi, C. Dual enhancement of electroluminescence efficiency and operational stability by rapid upconversion of triplet excitons in OLEDs. *Sci. Rep.* **5**, 8429 (2015).
7. Kikuchi, A., Nakabai, Y., Oguchi-Fujiyama, N., Miyazawa, K. & Yagi, M. Energy-donor phosphorescence quenching study of triplet-triplet energy transfer between UV absorbers. *Journal of Luminescence* **166**, 203–208 (2015).
8. D'Andrade, B. W., Datta, S., Forrest, S. R., Djurovich, P., Polikarpov, E. & Thompson, M. E. Relationship between the ionization and oxidation potentials of molecular organic semiconductors. *Organic Electronics* **6**, 11–20 (2005).
9. Romero, N. A. & Nicewicz, D. A. Organic photoredox catalysis. *Chem Rev.* **14**, 10075–10166 (2016).
10. Chatterjee, S. *et al.* Photochemistry of carbocyanine alkyltriphenylborate salts: intra-ion-pair electron transfer and the chemistry of boranyl radicals. *J. Am. Chem. Soc.* **112**, 6329–6338 (1990).
11. Maafi, M. & Brown, R. G. The kinetic model for AB(1φ{symbol}) systems. A closed-form integration of the differential equation with a variable photokinetic factor. *J. Photochem. Photobiol. A Chem.* **187**, 319–324 (2007)
12. Watts, D. C. Reaction kinetics and mechanics in photo-polymerised networks. *Dent. Mater.* **21**, 27–35 (2005).
13. Costentin, C., Robert, M. & Savéant, J. M. Electron transfer and bond breaking: recent advances. *Chem. Phys.* **324**, 40–56 (2006).
14. Koyama, D., Dale, H. J. A. & Orr-Ewing, A. J. Ultrafast observation of a photoredox reaction mechanism: photoinitiation in organocatalyzed atom-transfer radical polymerization. *J. Am. Chem. Soc.* **140**, 1285–1293 (2018).
15. Romańczyk, P. P. & Kurek, S. S. Reliable reduction potentials of diaryliodonium cations and aryl radicals in acetonitrile from high-level ab initio computations. *Electrochim. Acta* **351**, 136404 (2020).
16. Pause, L., Robert, M. & Savéant, J. M. Stepwise and concerted pathways in photoinduced and thermal electron-transfer/bond-breaking reactions. Experimental illustration of similarities and contrasts. *J. Am. Chem. Soc.* **123**, 4886–4895 (2001).
17. Pan, X. *et al.* Mechanism of photoinduced metal-free atom transfer radical polymerization: experimental and computational studies. *J. Am. Chem. Soc.* **138**, 2411–2425 (2016).
18. Hu, J., Wang, J., Nguyen, T. H. & Zheng, N. The chemistry of amine radical cations produced by visible light photoredox catalysis. *Beilstein J. Org. Chem.* **9**, 1977–2001 (2013).
19. Yu, C. *et al.* Defect-free acrylic polymers with a near-poisson distribution prepared via catalyst-free visible-light-driven radical polymerization. *ChemRxiv* doi:10.26434/chemrxiv-2023-dl842 (2023).